Scientific Reports

https://doi.org/10.1038/s41598-026-61586-4

Article in Press

# Degradation-aware PSO–MPC energy management for second-life battery prosumer microgrids

Received: 8 May 2026

Accepted: 6 July 2026

Published online: 27 July 2026

Cite this article as: Terkes M., Demirci A., Dagal I. *et al.* Degradation-aware PSO–MPC energy management for second-life battery prosumer microgrids. *Sci Rep* (2026). https://doi.org/10.1038/s41598-026-61586-4

Musa Terkes, Alpaslan Demirci, Idriss Dagal, Erdin Gokalp & Umit Cali

We are providing an unedited version of this manuscript to give early access to its findings. Before final publication, the manuscript will undergo further editing. Please note there may be errors present which affect the content, and all legal disclaimers apply.

If this paper is publishing under a Transparent Peer Review model then Peer Review reports will publish with the final article.

ARTICLE IN PRESS

© The Author(s) 2026. **Open Access** This article is licensed under a Creative Commons Attribution 4.0 International License, which permits use, sharing, adaptation, distribution and reproduction in any medium or format, as long as you give appropriate credit to the original author(s) and the source, provide a link to the Creative Commons licence, and indicate if changes were made. The images or other third party material in this article are included in the article's Creative Commons licence, unless indicated otherwise in a credit line to the material. If material is not included in the article's Creative Commons licence and your intended use is not permitted by statutory regulation or exceeds the permitted use, you will need to obtain permission directly from the copyright holder. To view a copy of this licence, visit http://creativecommons.org/licenses/by/4.0/.

ARTICLE IN PRESS

# Degradation-Aware PSO–MPC Energy Management for Second-Life Battery Prosumer Microgrids

Musa Terkes[1] | , Alpaslan Demirci[1] | , Idriss Dagal[2] | , Erdin Gokalp[1] | , Umit Cali[3,4,5] |

1. Department of Electrical Engineering, Yildiz Technical University, İstanbul, Türkiye.
2. Department of Electrical-Electronics Engineering, Istanbul Beykent University, 34396 Istanbul, Türkiye
3. Department of Electric Energy, Norwegian University of Science and Technology, Trondheim, Norway
4. School of Physics, Engineering and Technology, University of York, York, United Kingdom
5. American University of Sharjah, Artificial Intelligence, Smart Infrastructure and Robotics Research Center, Sharjah, United Arab Emirates

**Correspondence:**

[3]Umit Cali, Department of Electric Energy, Norwegian University of Science and Technology, Trondheim, Norway

**Email:** umit.cali@ntnu.no

ARTICLE IN PRESS

**ABSTRACT**

The growing retirement of electric vehicle lithium-ion batteries has created significant opportunities for their reuse in stationary energy storage systems. However, integrating second-life batteries (SLBs) into residential photovoltaic (PV)-based prosumer microgrids remains challenging due to heterogeneous initial state-of-health (SoH) conditions, accelerated degradation behavior, and uncertain remaining useful life. This paper proposes a degradation-aware energy management framework for SLB-integrated prosumer microgrids based on the joint use of particle swarm optimization (PSO) and model predictive control (MPC). The proposed framework consists of four coordinated stages: PSO-based capacity sizing, hybrid AI-based forecasting of PV generation, electricity prices, and load demand, SoH-aware adaptive battery management within the MPC layer, and net present value (NPV)-based battery replacement decision-making. Within the control layer, the adaptive battery management mechanism updates state-of-charge limits, C-rate constraints, and degradation penalty coefficients according to real-time SoH evolution, thereby mitigating excessive capacity fade while preventing economically inefficient underutilization. In addition, a three-stage replacement strategy is developed to determine whether continued operation, second-life battery replacement, or fresh battery replacement yields the highest long-term economic benefit. The proposed method is evaluated through long-horizon simulations using 2024 meteorological, market, and demand data for five residential prosumers in Antalya, Türkiye. The results show that the framework achieves a

ARTICLE IN PRESS

fleet-average self-consumption ratio of 71.8%, a renewable energy penetration factor of 37.6%, and a cost of energy of 0.0722 $/kWh, while sustaining battery utilization and enabling lifecycle-aware operation under realistic uncertainty. These findings demonstrate that the proposed PSO–MPC framework provides a computationally tractable approach that achieved stable convergence and feasible MPC solve times (2.1–3.4 s per 72-hour horizon) across all 20 simulated years under the five-prosumer Antalya configuration for degradation-aware energy management of second-life battery microgrids.

**Keywords:** Second-life battery; model predictive control; particle swarm optimization; state of health; prosumer microgrid; battery degradation.

**Nomenclature**

| | |
|---|---|
| $P_{k,t}^{ch}, P_{k,t}^{dch}$ | Charging and discharging power of prosumer $k$ at time $t$ (kW) |
| $E_{k,t}$ | Stored energy (state of energy) of battery for prosumer $k$ at time $t$ (kWh) |
| $P_{k,t}^{grid}$ | Net grid power exchange of prosumer $k$ at time $t$; positive = import, negative = export (kW) |
| $P_{k,t}^{PV\to load}$, $P_{k,t}^{PV\to bat}$, $P_{k,t}^{PV\to grid}$ | PV power allocated to load, battery charging, and grid export (kW) |
| $P_k^{PV}$ | Installed PV capacity of prosumer $k$ (kW) |
| $E_k^{ESS}$ | Nominal ESS capacity of prosumer $k$ (kWh) |
| $\eta_k^{init}$ | Initial state of health of prosumer $k$'s battery |
| $\eta_k(t)$ | Time-varying state of health of prosumer $k$'s battery |
| $\eta^{EoL}$ | EoL SoH threshold (0.50 for SLB, 0.60 for FB) |
| $E_k^{eff}(t)$ | Effective (usable) battery capacity at time $t$ (kWh) |
| $\pi_t^{grid}$ | Time-varying grid electricity price ($/kWh) |
| $\pi^{FiT}$ | Fixed feed-in tariff ($/kWh) |
| $r$ | Annual discount rate |
| $\varphi$ | Annual inflation rate |
| $\alpha^{deg}$ | Degradation acceleration factor for SLBs (= 1.8) |
| $C^{SLB}, C^{fresh}$ | Unit capital cost of second-life / fresh battery ($/kWh) |
| $C_{SLB}^{O\&M}, C_{FB}^{O\&M}$ | Annual O&M cost of SLB / fresh battery ($/kWh·yr) |
| $\sigma^{SoH}$ | SoH uncertainty band (±%) |
| $T_k^{expexted}$ | Expected battery service lifetime before EoL (yr) |
| $NPV_k^{ESS}$ | Net present value of ESS investment for prosumer $k$ ($) |
| $LCOE_k^{PV}$, $LCOE_k^{INV}$, $LCOE_k^{ESS}$ | Levelized cost of energy for PV, inverter, and ESS ($/kWh) |
| $v_p^i, x_p^i$ | Particle velocity and position in PSO at iteration $i$ |
| $w^i$ | Inertia weight of PSO at iteration $i$ |
| $c_1, c_2$ | PSO cognitive and social acceleration coefficients |
| $p_{best,p}, g_{best}$ | Personal best and global best positions in PSO |

**Abbreviations**

| | |
|---|---|
| ABM | Adaptive Battery Management |
| CAPEX | Capital Expenditure |
| CEEMDAN | Complete Ensemble Empirical Mode Decomposition with Adaptive Noise |
| COE | Cost of Energy |
| DHI | Diffuse Horizontal Irradiance |
| DNI | Direct Normal Irradiance |
| EMS | Energy Management System |
| EoL | End of Life |
| EPİAŞ | Energy Exchange İstanbul |
| ESS | Energy Storage System |
| EV | Electric Vehicle |
| FB | Fresh Battery |
| FiT | Feed-in Tariff |
| GBR | Gradient Boosting Regressor |
| GHI | Global Horizontal Irradiance |
| IMF | Intrinsic Mode Function |
| LCOE | Levelized Cost of Electricity |
| LSTM | Long Short-Term Memory |
| MAPE | Mean Absolute Percentage Error |
| MC | Monte Carlo |
| MIPGap | Mixed-Integer Programming Optimality Gap |
| MLP | Multi-Layer Perceptron |
| MPC | Model Predictive Control |
| nMAE | Normalized Mean Absolute Error |
| NPV | Net Present Value |

ARTICLE IN PRESS

| Nomenclature | |
|---|---|
| $X_t$ | Input feature sequence matrix for LSTM ( $R^{\{24x18\}}$) |
| $h_t$ | LSTM hidden state vector at time t ($R^{64}$) |
| $f_t, i_t, o_t$ | LSTM forget, input, and output gate activations |
| $C_t$ | LSTM cell state at time t |
| $\alpha_t$ | Attention weight assigned to hidden state at time t |
| $c$ | Attention context vector |
| $\tilde{y}_t^{LSTM}$, $\tilde{y}_t^{XGB}$, $\tilde{y}_t^{PV}$ | Intermediate LSTM, XGBoost, and final PV forecast (kW) |
| $\bar{y}_t, \sigma_t^2$ | Mean and variance from Monte Carlo dropout ensemble |
| $J_{MPC}$ | MPC objective function (total cost over 72-hour horizon) ($) |
| $C_{k,t}^{grid}, C_{k,t}^{deg}$, $C_{k,t}^{tp}, C_{k,t}^{cap}$ | Grid cost, degradation penalty, throughput penalty, and capital cost terms ($/h) |
| $R_{k,t}^{FiT}$ | Feed-in tariff revenue at time t ($) |
| $w_k^{deg(\eta,k)}$, $w_k^{tp(\eta,k)}$ | SoH-dependent degradation and throughput penalty weights |
| $\Phi^{deg}$ | Degradation cost function value |
| $\beta_k^{tp}$ | Throughput penalty scaling coefficient |
| $\Phi_k^{util}$ | Annual utilization penalty term ($) |
| $\lambda^{util}$ | Utilization penalty cost coefficient ($/kWh) |
| $U^{target}$ | Annual effective capacity utilization target (0.50) |
| $SoC_k^{min(\eta,k)}$, $SoC_k^{max(\eta,k)}$ | Adaptive lower and upper SoC bounds as a function of SoH |
| $C_k^{max(\eta,k)}$ | Adaptive maximum C-rate limit as a function of SoH |
| $\eta^{ch}, \eta^{dch}$ | Battery charging and discharging efficiency |
| $b_{k,t}^{tot}, b_{k,t}^{cyc}, b_{k,t}^{cal}$ | Total, cycle-induced, and calendar-induced degradation |
| $L^{cyc}, L^{cal}$ | Cycle life and calendar life reference parameters (cycles / h) |
| $\kappa_1, \kappa_2$ | Empirical calendar aging coefficients |
| $SoF_k^{energy}$, $SoF_k^{power}$, $SoF_k^{eventual}$ | Energy-based, power-based, and composite state of function |
| $w_E, w_P$ | Weighting coefficients for composite SoF |
| $\bar{U}_k$ | Trailing one-year average battery utilization rate |
| $T^{remain}$ | Remaining project lifetime from current year |
| $NPV_k^{continue}$, $NPV_k^{SLB}$, $NPV_k^{fresh}$ | NPV of continuing, SLB replacement, and fresh battery scenarios ($) |
| $\Psi_y^{util}$ | Annual utilization penalty in NPV scenario evaluation ($/yr) |

| Abbreviations | |
|---|---|
| O&M | Operation and Maintenance |
| OPEX | Operational Expenditure |
| PSO | Particle Swarm Optimization |
| PV | Photovoltaic |
| RF | Renewable Energy Penetration Factor |
| RMSE | Root Mean Square Error |
| RuL | Remaining Useful Life |
| SCR | Self-Consumption Ratio |
| SEI | Solid Electrolyte Interphase |
| SLB | Second-Life Battery |
| SMP | System Marginal Price |
| SoC | State of Charge |
| SoF | State of Function |
| SoH | State of Health |
| SSR | Self-Sufficiency Ratio |
| ToU | Time-of-use |
| XGBoost | eXtreme Gradient Boosting |
| YAL / YAT | Load Increase / Load Decrease Instruction (Turkish electricity market) |

| Nomenclature | |
|---|---|
| $\eta^{new}$ | Initial SoH of replacement battery |
| $CA_k(t)$ | Capacity aging metric at time t (%) |
| $SCR_k, SSR_k$ | Self-consumption ratio and self-sufficiency ratio of prosumer k (%) |
| RF | System-wide renewable energy penetration factor (%) |
| $CO_2^{total}$ | Total operational $CO_2$ emissions from grid imports (kg) |
| $CF_t$ | PV capacity factor at time t |
| M | Big-M constant for binary coupling constraints (kW) |
| $u_{k,t}^{z1}, u_{k,t}^{z2}$ | Binary variables for import/export and charge/discharge mode selection |
| K | Number of prosumers (= 5) |
| $\beta, \gamma$ | Exponential degradation weight tuning parameters ($\beta$ = 149, $\gamma$ = 15) |

## 1. INTRODUCTION

ARTICLE IN PRESS

The accelerating global transition toward electric mobility has created an unprecedented challenge in battery lifecycle management. As electric vehicle (EV) adoption intensifies, lithium-ion batteries are typically retired from vehicular service when their capacity degrades to approximately 70-80% of their nominal value [1,2]. However, these retired batteries retain substantial residual capacity and can serve effectively in less demanding stationary energy storage applications, presenting both environmental and economic opportunities [3,4]. The integration of second-life batteries (SLBs) with distributed photovoltaic (PV) systems offers a promising pathway to extend battery utility, reduce waste, and improve the economic viability of residential and community-scale microgrids [5,6].

Despite their potential, the deployment of SLBs in grid-connected energy systems introduces significant technical and operational complexities that have not been adequately addressed in existing literature [7,8]. Unlike fresh batteries (FBs) with predictable degradation trajectories and homogeneous performance characteristics, SLBs exhibit substantial heterogeneity in initial state of health (SoH), degradation rates, and capacity distributions due to varying first-life operational histories [9,10]. This heterogeneity fundamentally challenges conventional energy management strategies that assume uniform battery behavior and static operational constraints [11]. Furthermore, the economic assessment of SLB systems requires careful consideration of repurposing costs, uncertain remaining useful life (RuL), and the trade-off between extended utilization and accelerated degradation [1,12].

### 1.1. Motivation and Problem Statement

The primary motivation for developing advanced energy management systems (EMS) for SLB-integrated microgrids stems from the substantial gap between the theoretical sustainability benefits of battery reuse and the practical challenges of achieving reliable, economically viable operation [13,14]. Sustainability evaluation frameworks have demonstrated that SLBs with high initial SoH (above 75%) and slow degradation rates exhibit superior performance across economic, environmental, and social dimensions [1]. Techno-economic analyses in developing regions have shown that SLB-powered PV systems can reduce levelized cost of electricity (LCOE) by 5.6-35.3% compared to new battery systems, with payback periods shortened by 8.2-42.9% [2]. These findings establish a compelling economic case for SLB deployment, particularly in cost-sensitive applications such as rural electrification and community energy access [15,16].

However, realizing these benefits in practice requires addressing several critical technical challenges. First, the capacity mismatch among SLB cells, often exceeding 15% of nominal values due to uneven first-life degradation, significantly reduces usable system capacity and round-trip efficiency [12]. Dynamic equalization techniques employing active balancing architectures have demonstrated capacity improvements of approximately 16% through intelligent charge redistribution, yet such approaches introduce additional complexity and cost [12]. Second, the accelerated degradation characteristics of SLBs, which typically degrade 1.5-2× faster than FBs under identical operational conditions [4,17], necessitate adaptive control strategies that can dynamically adjust operational limits based on evolving battery health.

The economic viability of SLB systems is fundamentally dependent on achieving sufficiently high utilization rates while simultaneously managing degradation to ensure acceptable service life [18]. Studies on commercial building applications have shown that

ARTICLE IN PRESS

multi-timescale control frameworks can achieve 28.6% electricity cost reduction with annual degradation rates limited to 1.20%, yielding payback periods of approximately 5 years [17]. However, these results were obtained under carefully designed health-preserving constraints including restricted state-of-charge (SoC) windows (15-85%) and conservative C-rate limits (0.25C) [17]. The critical question remains: how can SLB systems be operated to maximize economic value and renewable energy utilization without entering an "underutilization regime, defined as annual throughput below 50% of effective capacity" characterized by minimal usage due to overly conservative protection strategies? [19]

Recent research has identified that maintaining sufficiently high battery utilization levels is essential for ensuring both economic competitiveness and meaningful contribution to grid services [9,20]. Field demonstrations of microgrid systems utilizing retired Nissan Leaf batteries showed that despite initial SoH averaging only 71%, substantially below the commonly cited 80% retirement threshold, the systems achieved 39% reduction in peak-time energy use and 60% reduction in peak demand when operated with appropriate control strategies [20]. These results challenge conventional assumptions about SLB viability and suggest that well-designed EMS frameworks can extract significant value even from heavily degraded batteries [21].

### 1.2. Limitations of Existing Approaches

A comprehensive analysis of current SLB energy management methodologies reveals several persistent limitations that constrain practical deployment. First, while model predictive control (MPC) has been widely adopted for battery energy storage systems due to its ability to handle constraints and forecasts naturally [13,22], most existing MPC formulations for SLB applications rely on static battery constraints and do not explicitly reshape the feasible operating region as SoH evolves. In contrast to formulations that treat SoH as a fixed scalar multiplier on capacity [5,23], or that adapt degradation cost coefficients without modifying the operational envelope [24,25], the proposed ABM mechanism introduces SoH-zone-contingent modifications to both the admissible SoC window and the maximum C-rate ceiling, creating a control law whose feasible region is itself a function of the evolving battery state. This distinction is mechanistically significant: shifting penalty weights alone cannot prevent high-DoD cycling near end-of-life if the SoC bounds remain unchanged, and the literature confirms that capacity fade accelerates nonlinearly within the final 15% of usable SoH [26]. Risk-based scheduling approaches incorporating Weibull distribution models for SLB failure probability have demonstrated improved reliability compared to deterministic methods [5], yet these frameworks still rely on fixed degradation cost functions that fail to capture the nonlinear relationship between operational stress and capacity fade in aged batteries [27].

Second, the mathematical representation of SLB degradation within optimization frameworks remains oversimplified in most studies [28]. Electrochemical models coupling degradation mechanisms, including solid electrolyte interphase (SEI) growth and lithium plating, with economic optimization have shown that parallel battery configurations can slow degradation while maintaining power delivery [4]. However, such physics-based models introduce computational complexity incompatible with real-time control, with solution times ranging from several minutes to hours depending on system scale [4,17]. Conversely, simplified degradation representations using linear capacity loss assumptions or fixed

ARTICLE IN PRESS

replacement schedules fail to capture the coupled effects of calendar and cycle aging under variable SoH conditions [9,29].

Third, existing economic evaluation frameworks for SLB systems often neglect critical factors influencing long-term profitability. Life cycle assessment studies have demonstrated that repurposing strategies significantly impact environmental performance, with benefits ranging from 33-44% reduction in carbon footprint depending on component reuse decisions [6]. Yet most techno-economic analyses assume fixed SLB pricing models without accounting for the dynamic relationship between initial SoH, expected lifetime, and economic value [1,9]. Comprehensive pricing models incorporating resourcing costs, repurposing expenses, and SLB market dynamics have projected prices ranging from 23-67 $/kWh depending on regional markets and initial battery conditions [1]. The economic viability analysis must integrate these variable costs with uncertain degradation trajectories to enable robust investment decisions [11].

Fourth, the treatment of battery heterogeneity and state-of-function (SoF) considerations has received limited attention in SLB control literature [30]. Hierarchical energy management frameworks for community microgrids have shown that coordinated optimization across multiple residential users can balance social welfare, battery lifetime, and grid integration objectives through many-objective formulation [10]. However, such approaches typically assume homogeneous battery modules and do not address the SoC balancing challenges arising from capacity mismatch in repurposed battery packs [31]. Dual-stage MPC strategies employing SoC-dependent power distribution for delta-connected cascaded H-bridge converters have achieved effective balancing among heterogeneous SLB modules, demonstrating that advanced control architectures can manage cell-level variations [31]. Nevertheless, these power electronics solutions add significant system cost and complexity.

Fifth, the temporal granularity and optimization horizon employed in existing studies often fail to capture realistic operational dynamics. While annual deterministic optimization provides theoretical insights into long-term system behavior [23,29], such approaches assume perfect foresight of generation, demand, and pricing, conditions unattainable in practice. Robust and decentralized optimization frameworks have been proposed to explicitly address multiple sources of uncertainty in multi-energy microgrids, improving operational resilience under uncertain renewable generation, load demand, and market conditions [32]. Nevertheless, these approaches generally focus on system-level economic and environmental objectives rather than incorporating dynamic SoH-dependent operational constraints for second-life batteries. Multi-timescale control frameworks decomposing the problem into hourly energy arbitrage and real-time peak shaving have demonstrated computational tractability with sub-500 ms solution times [17], yet the interaction between short-term operational decisions and long-term battery aging remains poorly understood. The fundamental question of whether day-ahead or weekly MPC horizons deliver superior lifecycle performance compared to longer planning periods has not been systematically investigated for SLB systems.

Finally, the integration of machine learning techniques with MPC for SLB applications remains nascent despite promising results in other domains. Regression-based error compensation methods combining physics-based building models with data-driven residual estimators have achieved model error reductions of 56-80% in hierarchical MPC systems [33]. Similarly, multi-objective optimization frameworks embedding control-oriented

ARTICLE IN PRESS

physical aging models within dynamic programming solvers have demonstrated simultaneous reduction in electricity bills and battery degradation for residential microgrids [29]. However, these hybrid approaches have not been extended to SLB systems where model uncertainty is inherently higher due to unknown first-life operational history and accelerated degradation dynamics [15,34]. Recent surveys of SLB research have identified accurate SoH estimation, optimization of application-specific health indicators, and incorporation of first-life degradation data as critical technical gaps [35]. The lack of standardized business models, absence of FB history, and insufficient policy frameworks for SLB deployment compound these technical challenges [35,36]. Techno-economic studies comparing SLBs to new batteries in domestic renewable energy installations have shown that while capital costs are reduced by 75%, the economic viability depends critically on achieving realistic utilization rates and managing safety risks through appropriate system design [36]. Supporting sustainable development goals through SLB deployment requires addressing these multifaceted challenges through integrated technical and economic frameworks [37].

### 1.3. Research Objectives and Contributions

This study addresses the identified gaps by developing a comprehensive MPC-based EMS framework specifically designed for SLB-integrated PV systems in residential prosumer applications. The primary objective is to establish operational strategies that maximize the economic and environmental value of SLBs while ensuring safe, reliable operation through SoH-aware adaptive control mechanisms. Unlike conventional approaches treating battery management as purely a cost minimization problem, this work reconceptualizes SLB energy management as a multi-dimensional sustainability challenge where utilization rate, degradation control, and renewable energy integration must be simultaneously optimized. The research explicitly addresses the critical requirement of achieving sufficiently high SLB utilization levels to justify system deployment from both economic and environmental perspectives, emphasizing the need for enhanced and sustained utilization performance [2,9]. This condition reflects the level of energy throughput required to achieve competitive LCOE relative to fresh battery alternatives and to offset the embodied energy and carbon impacts associated with battery repurposing through sustained active utilization. The proposed framework employs adaptive operational constraints that dynamically adjust based on SoH evolution, thereby preventing the system from entering an economically inefficient underutilization regime despite remaining above conventional retirement thresholds [17,20]. At the power-electronics layer, multi-port DC architectures incorporating second-life storage also raise converter-level stability considerations, such as the dissipativity-based multiport stability root-cause analysis for solid-state transformers reported in [38]. The present study addresses the energy-management (scheduling) layer and does not model converter-level stability directly.

The specific contributions of this work are as follows:

- **SoH-aware adaptive battery management (ABM) for SLBs:** A degradation-aware adaptive control strategy is proposed that dynamically adjusts operational constraints according to real-time SoH evolution. The framework moves beyond static fresh-battery assumptions by introducing progressively evolving operational bounds tailored to SLB characteristics, thereby balancing utilization performance and degradation control. It extends aging-rate-aware MPC concepts [24,25] to explicitly

ARTICLE IN PRESS

address heterogeneous initial SoH conditions and accelerated degradation dynamics typical of SLBs [4,35].

- **Economically rational SLB replacement decision framework:** A dynamic battery replacement strategy based on net present value (NPV) analysis is developed to evaluate the trade-offs among continued SLB operation, SLB replacement, and fresh battery upgrade. Unlike fixed end-of-life criteria commonly adopted in the literature [1,5] the proposed framework integrates utilization behavior, SoH trajectory, and project horizon into the decision-making process, including mechanisms to detect inefficient low-utilization operating regimes [17,20].
- **Realistic long-term MPC-based lifecycle evaluation:** The proposed EMS is validated through long-term simulations employing short-horizon receding MPC rather than idealized annual optimization. This design captures forecasting uncertainty, path-dependent degradation, and the coupling between short-term operational decisions and long-term asset evolution, which are often neglected in deterministic planning studies [23,29].
- **Multi-objective optimization with utilization-oriented control:** A multi-objective MPC formulation is introduced that jointly considers operational cost, degradation impact, and energy throughput while promoting sufficiently high utilization levels for SLBs. The adaptive weighting structure enables the EMS to continuously adjust its operational priorities across different SoH regimes, preventing overly conservative strategies that undermine economic and environmental value creation [2,9,17,29].
- **Prosumer-centric comparative performance assessment:** The proposed adaptive strategy is systematically benchmarked against conventional EMS and battery-protection-oriented approaches across diverse residential prosumer profiles. The analysis quantifies trade-offs among economic performance, battery lifetime, and renewable energy utilization, demonstrating the advantages of user-adaptive control over generic management strategies [10,23,37].
- **Integrated techno-economic and environmental evaluation of SLBs:** A comprehensive assessment framework is developed that jointly incorporates SLB-specific cost structures, degradation dynamics, and environmental impacts. The results identify operating conditions under which SLBs can outperform fresh batteries in life-cycle economic and sustainability metrics, supported by sensitivity analyses across key techno-economic parameters [1,2,6,9,23].

The remainder of this article is organized as follows. Section 2 presents the SoH-aware MPC formulation, including degradation modeling and NPV-based decision logic. Section 3 reports the simulation and optimization results, including benchmark, ablation, and sensitivity analyses. Section 4 discusses the key implications, comparative findings, limitations, and future research directions. Section 5 concludes the paper.

## 2. METHODOLOGY

The proposed methodology establishes an integrated, degradation-aware decision-making framework for the optimal operation of second-life battery (SLB) systems in residential prosumer environments. Unlike conventional approaches that treat battery degradation as a passive or post-operational indicator, this study explicitly embeds state-of-health (SoH) dynamics into the control and optimization process, enabling adaptive and lifecycle-aware energy management. The framework combines predictive analytics, capacity optimization, and adaptive control within a unified closed-loop structure to jointly address operational

ARTICLE IN PRESS

efficiency, economic viability, and battery longevity. Specifically, hybrid AI-based models are employed to forecast PV generation, electricity prices, and load demand, while a particle swarm optimization (PSO) stage determines optimal system sizing parameters. These outputs are subsequently integrated into a model predictive control (MPC) framework enhanced with degradation awareness for real-time energy management. To capture long-term economic performance, a net present value (NPV)-based replacement mechanism is incorporated, enabling optimal battery replacement decisions under uncertainty. The proposed architecture addresses key challenges associated with SLBs, including heterogeneous initial SoH conditions, accelerated degradation behavior, and stochastic renewable generation and demand profiles. By tightly coupling forecasting, optimization, control, and economic evaluation, the framework ensures both real-time adaptability and long-term sustainability within a computationally tractable structure. The overall methodological workflow is illustrated in Figure 1, while the degradation-aware control and replacement logic are presented in Figure 2.

### 2.1. Integrated System Modeling and Operational Framework of the Prosumer Microgrid

The study investigates a residential prosumer microgrid composed of five households, each equipped with rooftop PV generation, SLB-based energy storage, and bidirectional grid connectivity. The system is analyzed over a 20-year operational horizon corresponding to 175,200 hourly timesteps. To maintain both computational tractability and forecasting reliability, the operational scheduling is implemented through a rolling model predictive control framework with sequential 72-hour horizons. Within this structure, each prosumer operates semi-autonomously while interacting with the main grid under time-varying electricity prices and locally enforced battery management constraints.

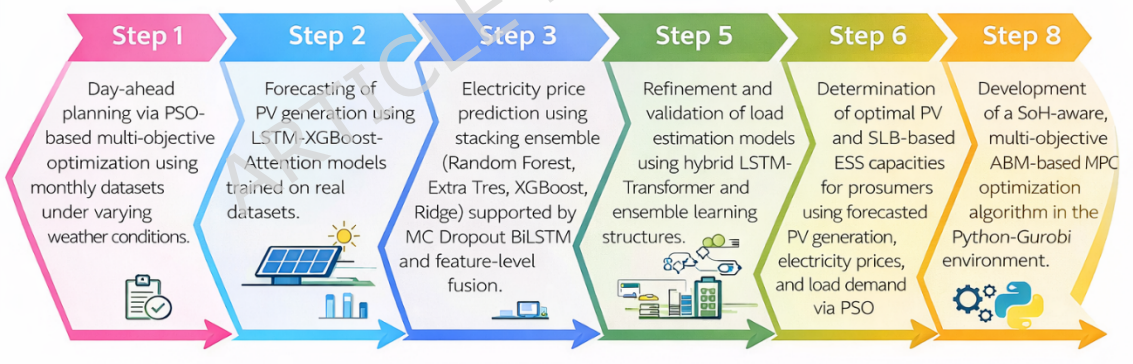



**Figure 1.** Multi-stage workflow integrating hybrid AI-based forecasting, PSO-based capacity optimization, and degradation-aware MPC development and implementation for energy management.

ARTICLE IN PRESS

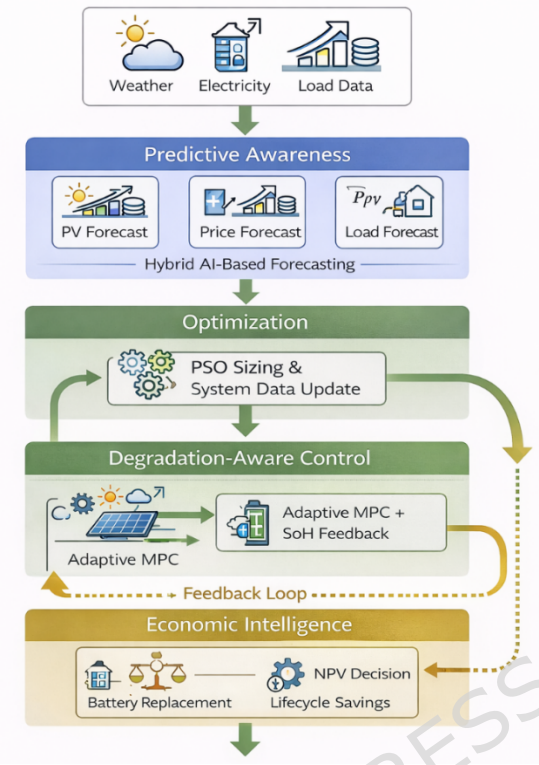



**Figure 2.** Hierarchical closed-loop energy management architecture integrating forecasting, PSO-based optimization, degradation-aware MPC with SoH feedback, and NPV-based economic decision-making.

At every timestep, the optimization determines the operational state of the storage system and the allocation of locally generated PV energy across competing uses. Charging and discharging actions are modeled as physically distinct processes to preserve directional consistency in energy flows, while the stored energy level is constrained by the physical limits of the battery system. Grid interaction is represented as a bidirectional exchange in which electricity can either be imported from or exported to the network. In parallel, PV generation is explicitly distributed among local demand supply, battery charging, and grid export, ensuring that all energy flows remain physically meaningful within the system representation. This formulation establishes a coherent energy management structure capable of capturing operational trade-offs among self-consumption, storage utilization, and market participation.

System sizing is determined through particle swarm optimization, which defines feasible capacity ranges for both PV installations and energy storage systems at the household level. The storage capacity upper bound is intentionally set slightly above that of a typical fresh battery to account for the reduced usable capacity associated with second-life systems. Unlike newly manufactured batteries, SLBs enter operation with heterogeneous health conditions due to their prior usage histories. Accordingly, the initial state of health of each battery is sampled from a bounded distribution rather than assumed identical across prosumers. As a result, the effective storage capacity becomes time-dependent and evolves with degradation over the project horizon, linking operational performance directly to battery aging dynamics.

Electricity trading between prosumers and the grid follows a time-of-use pricing structure for imports, while exports are compensated through a fixed feed-in tariff. The asymmetry

ARTICLE IN PRESS

between dynamic purchasing prices and a constant selling price introduces an economic spread that strongly influences scheduling decisions, particularly regarding when to store energy, self-consume PV production, or export surplus electricity. This market design therefore plays a central role in shaping optimal energy management strategies throughout the system lifetime.

Economic evaluation of the project is performed under macroeconomic assumptions specific to Türkiye, incorporating both a national discount rate and an annual inflation factor in long-term financial calculations. These parameters are embedded into all cost assessments to ensure realistic valuation of investment and operational decisions over the 20-year horizon and to properly capture intertemporal trade-offs between upfront system sizing and future operational savings.

Particular emphasis is placed on the characterization of second-life batteries, which differ fundamentally from fresh batteries in both performance uncertainty and cost structure. Because SLBs inherit unknown first-life degradation histories, their modeling requires stochastic initial conditions and accelerated aging behavior relative to new batteries. The adopted degradation acceleration factor reflects the faster capacity fade typically observed in repurposed systems. Although SLBs offer a substantially lower capital cost than fresh batteries, this advantage is partially offset by higher operation and maintenance expenses and greater uncertainty in state-of-health estimation. In addition, the end-of-life threshold is defined at a lower capacity retention level than that commonly used for new batteries, reflecting the extended utilization philosophy associated with second-life applications. Collectively, these assumptions enable the framework to realistically capture the economic and operational implications of integrating second-life storage into residential prosumer microgrids while maintaining methodological rigor suitable for long-term system analysis.

## 2.2. Stage I: Capacity Optimization via PSO

### 2.2.1. Objective Function Formulation

Equation (1) defines the PSO objective as the minimization of the aggregated 20-year levelized cost of electricity across all prosumers. The cost function integrates PV system costs, inverter costs, and energy storage costs, thereby capturing the full techno-economic footprint of the hybrid configuration. The decision vector simultaneously optimizes storage capacities and PV power ratings for all prosumers, resulting in a 10-dimensional search space. The upper bound of 10 kWh applies to the effective usable capacity at installation; the corresponding upper bound on nominal ESS capacity is set at 20 kWh to permit full compensation for initial SoH heterogeneity, as the optimizer must provision sufficient nominal capacity to deliver the required effective throughput after the initial SoH discount is applied. Lower bounds prevent negative sizing decisions, and PV capacity is constrained to 15 kW per prosumer. Together, these formulations define a constrained multi-variable optimization problem that balances long-term economic performance with practical design limits.

$$\min_{x} J_{PSO} = \sum_{k=1}^{K} \left[ LCOE_k^{PV} + LCOE_k^{INV} + LCOE_k^{ESS} \right] \quad (1)$$

ARTICLE IN PRESS

$$LCOE_k^{PV} = \frac{-\left(-C_0^{CAPEX,\,PV} - \sum_{y=1}^{20} \frac{C_y^{O\&M,PV}}{(1+r)^y}\right)}{\sum_{y=1}^{20} E_{k,y}^{PV}} \tag{2}$$

$$LCOE_k^{INV} = \frac{-\left(-P_k^{INV}.Cap_k^{INV}\right)}{\sum_{y=1}^{20} E_{k,y}^{PV}} \tag{3}$$

Equation (2) defines the levelized cost of PV generation by amortizing the net present value of PV investments over the total lifetime energy production. The net present value accounts for the initial capital expenditure and the discounted stream of annual operation and maintenance costs. Capital cost is linearly proportional to installed PV capacity while annual O&M expenses are modeled as a fixed 1% fraction of the initial investment. Inverter sizing follows the conventional oversizing ratio given in Equation (3), ensuring compatibility between DC PV capacity and AC conversion limits. Similar to the PV calculation, the inverter levelized cost is derived by spreading its net present value over cumulative PV energy output. Since inverter investment is treated as an upfront cost without additional annual components, its net present value simplifies to the capital term. Together, these formulations provide a consistent NPV-based cost allocation framework for both generation and power conversion assets over the 20-year project horizon.

### 2.2.2. SLB-Specific NPV Calculation with Replacement Logic

Equation (4) formulates the NPV of the SLB by incorporating initial investment, discounted operating expenses, and stochastic replacement costs arising from degradation-driven end-of-life events. The initial capital cost is based on the effective available capacity rather than nominal capacity, thereby directly linking investment size to the battery's initial SoH. The expected service lifetime prior to reaching the EoL threshold is modeled in Equation (5) as a function of the initial health condition, ensuring that higher initial SoH values translate into longer usable lifetimes, with an upper bound of the 20-year project horizon. Replacement events are scheduled at intervals corresponding to the expected lifetime of the component. At each of these intervals, except during the final year of the project horizon, a replacement cost is applied that reflects reductions associated with technological learning and cost evolution over time (Equation (6)). Finally, the levelized cost of storage is calculated by distributing the total discounted cost over the cumulative operational hours of the 20-year period. This structure captures both economic and degradation-driven uncertainties in second-life battery deployment within a unified NPV-based framework.

$$NPV_k^{ESS} = -E_{k,0}^{eff}.C^{SLB} - \sum_{y=1}^{20} \frac{C_y^{O\&M,ESS} + C_y^{replace}}{(1+r)^y} \tag{4}$$

$$T_k^{expected} = \min\left(20, \left\lfloor \frac{8.\left(\eta_k^{init} - \eta^{EoL}\right)}{1-\eta^{EoL}} \right\rfloor\right) \tag{5}$$

$$C_y^{replace} = \begin{cases} 0.90.C^{SLB}.E_{k,0}^{eff} & \text{if } y \equiv 0 \left(\text{mod } T_k^{expected}\right) \text{ and } y < 20 \\ 0 & \text{otherwise} \end{cases} \tag{6}$$

### 2.2.3. PSO Algorithm Implementation

ARTICLE IN PRESS

Equation (7) defines the velocity update rule of the particle swarm optimization algorithm within the 10-dimensional design space. The new velocity is composed of three components: an inertia term weighted by $w^i$, a cognitive term guiding the particle toward its personal best position $p_{best,p}$, and a social term directing it toward the global best solution $g_{best}$. The inertia weight decreases linearly from 0.9 to 0.4 to gradually shift the search from exploration to exploitation, while the acceleration coefficients are fixed at $c_1 = c_2 = 2.0$. The random vectors $r_1, r_2 \sim U(0,1)$ introduce stochasticity, and the operator $\odot$ denotes element-wise multiplication. Equation (8) then updates the particle position by adding the newly computed velocity to the current position. At each iteration, fitness values are evaluated using the objective function defined in Equation (1). For every particle configuration, the MPC framework is executed over a full operational year using actual 2024 PV generation, load demand, and electricity price data. The resulting annual operating cost is combined with the corresponding levelized capital costs to obtain the total fitness value. Personal and global best positions are updated accordingly, and the iterative process continues until convergence, as detailed in Algorithm 1.

$$v_p^{i+1} = w^i . v_p^i + c_1 . r_1 \odot \left( p_{best,p} - x_p^i \right) + c_2 . r_2 \odot \left( g_{best} - x_p^i \right) \tag{7}$$

$$x_p^{i+1} = x_p^i + v_p^{i+1} \tag{8}$$

### 2.3. Stage II: Hybrid AI-Based Forecasting

Accurate short-term predictions of PV generation ($\hat{P}_{k,t}^{PV}$), electricity prices ($\hat{\pi}_t^{grid}$), and load demand ($\hat{L}_{k,t}$) are critical for MPC performance. Three parallel forecasting models are deployed, each optimized for the specific characteristics of its target variable.

#### 2.3.1. PV Generation Forecasting

Accurate short-term forecasts of PV generation, electricity prices, and household demand are essential for the performance of the model predictive control framework. To address the distinct temporal characteristics of these variables, three forecasting models are developed in parallel. Among them, PV generation is predicted using a hybrid deep learning architecture specifically designed to capture nonlinear meteorological dependencies and temporal dynamics. For PV forecasting, the input at each timestep consists of a set of meteorological, temporal, and astronomical variables including different irradiance components, ambient temperature, wind speed, time indicators, seasonal encodings, and solar position parameters. A sliding-window sequence with a 24-hour look-back horizon is constructed and normalized using Min–Max scaling to stabilize the learning process. Temporal dependencies are extracted through a long short-term memory network that produces a compact latent representation of recent system dynamics. Rather than relying solely on sequential modeling, an attention mechanism is integrated to adaptively emphasize the most informative temporal patterns within the input sequence. This attention-enhanced representation is then processed through a dense layer to generate an initial prediction. To further improve predictive accuracy, the model adopts a hybrid ensemble structure in which the deep learning output is combined with the learned temporal context and provided as input to an XGBoost residual learner. This second stage refines the forecast by capturing nonlinear relationships that are not fully represented in the neural network component. The final PV generation estimate is obtained after reversing the normalization transformation.

ARTICLE IN PRESS

Predictive uncertainty is quantified using Monte Carlo Dropout, which performs multiple stochastic forward passes during inference to approximate the distribution of possible outcomes. The resulting ensemble predictions are used to compute the mean forecast, variance, and a 95% confidence interval, enabling the MPC framework to incorporate probabilistic information in operational decision-making. Using the 2024 Antalya dataset, the proposed hybrid LSTM–Attention–XGBoost architecture achieved an RMSE of 0.042 kW, a normalized MAE of 4.1%, and an $R^2$ value of 0.987. Moreover, the uncertainty estimation exhibited a 95% interval coverage of 94.2%, indicating both high predictive accuracy and well-calibrated probabilistic forecasts.

### 2.3.2. Electricity Price Forecasting

Electricity price forecasting is performed using a hybrid deep learning–ensemble framework designed to capture both temporal dependencies and nonlinear market dynamics. The input data consist of multiple market and system-level indicators, including the system marginal price (SMP), positive and negative imbalance prices, load increase and decrease instructions (YAL/YAT), and renewable generation variables such as wind and solar output, together with additional market signals. In total, 27 features are incorporated to represent short-term operational conditions in the electricity market. The primary forecasting component is based on a long short-term memory network trained to learn temporal patterns in price fluctuations. Monte Carlo Dropout is employed to enhance model robustness and improve generalization under volatile market conditions. While the LSTM captures sequential dependencies, additional machine learning models are introduced to exploit complementary nonlinear relationships that may not be fully represented in the recurrent architecture. To achieve this, a stacking ensemble is constructed using Random Forest, XGBoost, and multilayer perceptron models as base learners. Their outputs are combined with the LSTM prediction through a Ridge regression meta-learner, which performs the final aggregation. The regularization strength of the meta-learner is optimized using Bayesian hyperparameter search to improve validation performance and reduce overfitting. This ensemble structure allows the model to integrate temporal learning with tree-based and neural network representations, resulting in improved predictive stability under varying market regimes. The final electricity price forecast is obtained from the meta-learner that aggregates the predictions of all base models together with the processed feature representation. This hybrid configuration enhances forecasting reliability, particularly during periods of rapid price fluctuations. Using 2024 EPİAŞ market data, the proposed framework achieved an RMSE of 12.3 TL/MWh and a MAPE of 8.7%, while maintaining a peak-hour prediction accuracy of 91.2% within a ±10% tolerance band. These results indicate strong predictive capability under high-volatility conditions and confirm the effectiveness of combining deep learning with ensemble learning techniques for short-term electricity price forecasting.

### 2.3.3. Load Demand Forecasting

The load forecasting framework begins with signal decomposition to better capture the multi-scale characteristics of residential electricity consumption. Specifically, the raw household load profile is decomposed using CEEMDAN into a set of intrinsic mode functions together with a residual trend component representing long-term consumption behavior. To reduce noise while preserving meaningful consumption patterns, only the lower-frequency components are retained and reconstructed to form a denoised load signal used for subsequent modeling. Temporal forecasting is performed using a hybrid sequential architecture that combines recurrent and attention-based learning. A sliding time window is

ARTICLE IN PRESS

applied to the reconstructed load series and processed through an LSTM network to extract temporal dependencies in household demand. To further enhance representation capability, a self-attention mechanism is integrated, allowing the model to identify the most relevant temporal patterns and capture longer-range dependencies that conventional recurrent models may overlook. This hybrid LSTM–Transformer structure improves the model's ability to represent complex and irregular residential consumption dynamics. In addition to the sequential model, Gradient Boosting Regressor and multilayer perceptron models are trained in parallel to capture complementary nonlinear relationships within the input data. Their outputs are then combined using a RidgeCV-based meta-learner within a stacking ensemble framework, producing the final load demand forecast and improving robustness against individual model bias. The proposed CEEMDAN–LSTM–Transformer–stacking architecture was evaluated using the Pecan Street residential dataset covering 11 households. The model achieved an RMSE of 0.087 kW, a normalized MAE of 5.3%, and an $R^2$ value of 0.94, indicating strong generalization performance and stable forecasting accuracy across multiple households.

To contextualize the accuracy gains reported above, the accuracy of a naive day-ahead persistence forecast was also evaluated using the same load and PV datasets. In the persistence model, the forecast for hour $t$ was set equal to the realized value at hour $t - 24$. Persistence forecasting achieves $R^2 = 0.726$ for load and $R^2 = 0.889$ for PV generation, compared with $R^2 = 0.94$ and $R^2 = 0.987$, respectively, for the proposed hybrid architectures; for electricity price, persistence forecasting is markedly poor ($R^2 = 0.176$), motivating the market-aware ensemble used here. These comparisons indicate that the AI forecasting architectures provide a substantial, quantifiable accuracy improvement over a naive baseline.

The outputs of the three forecasting models serve as direct inputs to the MPC layer. Point forecasts of PV generation, load demand, and grid price over the 72-hour receding horizon populate the deterministic terms of the MPC objective (Equation 9). The Monte Carlo Dropout variance $\sigma_t^2$ for PV generation is propagated into the energy balance constraint as an additive safety reserve, preventing over-commitment of battery discharge under uncertain irradiance conditions: the scheduled discharge is reduced proportionally to the forecast standard deviation when it exceeds 10% of the mean generation estimate. Similarly, elevated price-forecast variance triggers a risk-averse scaling of the grid arbitrage term, reducing scheduled exports during high-volatility market intervals. This coupling ensures that forecast quality directly and quantifiably affects operational scheduling outcomes, and that the architectural complexity of the hybrid models is functionally justified.

## 2.4. Stage III: SoH-Aware ABM

### 2.4.1. MPC Formulation with Adaptive Constraints

The proposed control architecture employs an MPC framework operating on a rolling 72-hour optimization horizon that is updated every 24 hours. This structure allows the controller to continuously adapt operational decisions based on updated forecasts while maintaining computational feasibility. The optimization objective jointly considers grid electricity costs, degradation-aware penalties, energy throughput regulation, levelized capital cost allocation, and feed-in tariff revenues:

$$\min_{u} J_{MPC} = \sum_{k=1}^{K} \sum_{t=1}^{72} \left[ C_{k,t}^{grid}, C_{k,t}^{deg}, C_{k,t}^{tp}, C_{k,t}^{cap} - R_{k,t}^{FiT} \right] \quad (9)$$

ARTICLE IN PRESS

Grid electricity imports are priced according to the time-varying tariff structure, while exported PV generation produces revenue through a fixed feed-in tariff. To prevent excessive battery cycling, the optimization incorporates degradation and throughput penalties that dynamically depend on the SoH. As batteries age, the penalty weights increase, discouraging aggressive charge–discharge behavior and promoting longevity-oriented operation. In addition, a levelized capital cost component is embedded within the operational objective to internalize long-term investment costs into short-term scheduling decisions. A utilization control term is also introduced to prevent underuse of the storage system by enforcing a minimum annual throughput target, thereby avoiding an economically inefficient underutilization regime in which batteries remain idle due to conservative degradation penalties. System operation is governed by a set of physical constraints including energy balance, PV power allocation, and battery energy dynamics. The load of each prosumer must be satisfied through a combination of direct PV supply, battery discharge, or grid import, while PV generation is allocated among self-consumption, storage charging, grid export, or curtailment. Battery energy evolves according to charging and discharging efficiencies with hourly time resolution. A key feature of the framework is the introduction of SoH-adaptive operating constraints. As battery health declines, both the allowable SoC window and the maximum charging/discharging power are progressively tightened. This adaptive mechanism protects degraded batteries from operating in high-stress conditions that accelerate aging. In practice, the SoC range narrows and the allowable C-rate decreases across predefined SoH regions, ensuring that operational flexibility is gradually reduced as the battery approaches end-of-life. Additional operational constraints are imposed to reflect practical microgrid management policies. These include time-of-use restrictions that reserve stored energy for evening peak demand, limits on PV grid injection to avoid excessive export dependence, and binary coupling variables that prevent simultaneous charging and discharging or concurrent grid import and export. Together, these constraints ensure physically consistent and operationally realistic system behavior.

### 2.4.2. SLB Degradation Model

Battery degradation is modeled as the combined effect of cycle-induced and calendar-induced capacity loss. This formulation enables the framework to capture both usage-dependent aging and time-dependent degradation processes that are particularly relevant for second-life batteries. These two coupled recurrences are denoted throughout the remainder of the manuscript as Equations (10) and (11), respectively, and are cited under this same numbering in Sections 3.5, 4.3, and the Conclusions.

$$b_{k,t}^{cyc} = b_{k,t-1}^{total}\left(0.5\frac{L^{cal}}{L^{cyc}}\right) + 0.2.\alpha^{deg}\left(0.5\frac{\sum_{\tau=1}^{t}\left(P_{k,t}^{ch} + P_{k,t}^{dch}\right)}{E_k^{eff}.L^{cyc}}\right) \quad (10)$$

$$b_{k,t}^{cal} = b_{k,t-1}^{total}\left(1 - 0.5\frac{L^{cal}}{L^{cyc}}\right) + 0.2.\alpha^{deg}\sum_{\tau=1}^{t}\left[\kappa_1.SoC_{k,\tau} + \kappa_2\right] \quad (11)$$

Cycle degradation is driven by cumulative energy throughput relative to the effective battery capacity and cycle life, while calendar degradation depends on the time spent at different state-of-charge levels. To reflect the higher stress sensitivity of second-life batteries, the model incorporates an acceleration factor that amplifies degradation relative to fresh battery systems. The assumed cycle life is shorter than that of new batteries,

ARTICLE IN PRESS

reflecting the inherited aging of repurposed storage systems. The effective storage capacity is updated dynamically according to the accumulated degradation, and the battery state of health is recalculated at each timestep relative to the nominal installed capacity. This dynamic feedback allows the MPC controller to continuously adapt operational decisions as the battery condition evolves over time. To better represent battery performance limitations, two complementary indicators are defined: an energy-based state-of-function that reflects capacity retention and a power-related indicator that captures instantaneous deliverable capability. These metrics are combined into a composite health indicator that feeds back into the MPC constraints and degradation penalties, ensuring that operational strategies remain aligned with long-term battery sustainability.

In the present simulation framework, SoH at each timestep is derived directly from the recursive degradation model (Equations (10)–(11)), providing a continuous, noise-free state signal to the MPC controller without measurement noise. In a practical hardware deployment, this role would be fulfilled by an online SoH estimator, for example, an extended Kalman filter applied to a first-order equivalent circuit model, or a data-driven estimator incorporating first-life operational history. The accuracy of the SoH feedback signal directly governs the quality of adaptive constraint transitions; integrating a hardware-compatible estimator is identified as a key extension of this work (Section 4.4 and Conclusions). The primary contribution of the present study is the control and optimization architecture; SoH estimation is treated as a separately solvable sub-problem.

The coefficient 0.5 in the cycle/calendar split reflects the empirical finding that both aging mechanisms contribute approximately equally to total capacity fade under typical residential PV-storage duty cycles, where average SoC remains in the 40–70% range and daily depth-of-discharge is moderate [39]. Neubauer and Pesaran [39] report that calendar aging accounts for 45–55% of total capacity loss in stationary second-life applications under comparable duty cycles, providing a direct empirical anchor. The coefficient 0.2 scales the acceleration term such that, with $\alpha_{deg} = 1.8$, the overall degradation rate is approximately 1.8× that of a fresh cell under identical conditions, consistent with the 1.5–2× range documented for repurposed NMC cells with initial SoH in the 65–80% range [4,26]. Under representative operating conditions for the present study (nominal 1C charge rate, 50% mean SoC, approximately 18–20°C ambient consistent with Antalya's climate), the model produces an estimated annual first-year SoH loss of approximately 4.8%, in agreement with the 3–8%/yr range reported for NMC second-life cells in field and laboratory studies [26]. The absence of explicit Arrhenius temperature-dependent kinetics is a deliberate simplification appropriate for the mild and relatively uniform thermal climate of Antalya; its implications for model generalizability are discussed in Section 4.3 (Limitations).

#### 2.4.3. Adaptive Constraint Mechanisms

As battery degradation progresses, operation near extreme SoC levels can significantly accelerate electrochemical aging. Therefore, the admissible SoC window is gradually narrowed to reduce exposure to high-stress regions and improve long-term capacity retention. Similarly, the maximum allowable power level scales with the declining effective capacity while the permissible C-rate decreases with SoH, introducing an additional protection margin for aged batteries. Three SoH zones are used for this purpose, separated by the boundaries $\eta = 0.60$ (healthy/aging) and $\eta = 0.54$ (aging/critical), with a hard end-of-life threshold at $\eta = 0.50$ (Table 1). These boundary values were set by engineering judgement informed by the general second-life SoH-zoning practice reported in SoH- and

ARTICLE IN PRESS

temperature-aware adaptive SoC-boundary studies for second-life batteries [40] and in Ah-throughput-based degradation-cost management for second-life systems [41], rather than fitted directly to second-life NMC cycling data; Section 3.5 reports a dedicated sensitivity test on these specific boundaries.

$$\text{Window Width} = SoC_k^{max}(\eta_k) - SoC_k^{min}(\eta_k) = \begin{cases} 0.70 & \eta_k > 0.60 \\ 0.66 & 0.54 < \eta_k \le 0.60 \\ 0.60 & 0.50 < \eta_k \le 0.54 \\ 0.50 & \eta_k \le 0.50 \end{cases} \quad (12)$$

For applications requiring smoother transitions between health states, the degradation penalty can also be expressed through a continuous exponential function of SoH. However, the piecewise structure adopted in this study is preferred due to its interpretability and operational transparency across clearly defined degradation regimes.

$$w_k^{deg}(\eta_k) = 1 + \beta.\exp(-\gamma(\eta_k - \eta^{EoL})) \quad (13)$$

where $\beta = 149$ and $\gamma = 15$ are empirically tuned parameters. This exponential formulation provides smooth sensitivity near EoL, helping prevent underutilization while maintaining degradation awareness. Nevertheless, the piecewise structure defined earlier is preferred in practice due to its interpretability and deterministic behavior across clearly defined SoH regions. Finally, a utilization control mechanism ensures that the storage system remains economically active. If annual throughput falls below the target utilization level, a penalty term is activated within the MPC objective. This mechanism prevents overly conservative scheduling strategies and maintains a balance between degradation mitigation and effective asset utilization.

**Table 1.** SoH-zone-based adaptive operating envelope (SoC window and maximum C-rate) used by the SoH-aware ABM framework (Equation (12)).

| **SoH Zone** | **SoH Range (η)** | **SoC Window Width (Equation (12))** | **Max C-rate** |
|---|---|---|---|
| Healthy | $\eta > 0.60$ | 0.70 | 0.5C |
| Aging | $0.54 < \eta \le 0.60$ | 0.66 | 0.45C |
| Critical (usable) | $0.50 < \eta \le 0.54$ | 0.60 | 0.35C |
| Hard EoL | $\eta \le 0.50$ | 0.50 | 0.25C |

ARTICLE IN PRESS

### 2.5. Stage IV: NPV-Based Battery Replacement Logic

#### 2.5.1. Replacement Decision Framework

Battery replacement decisions are governed by a hierarchical framework that integrates technical end-of-life limits, operational utilization patterns, and long-term economic optimization. This structure ensures that replacement actions remain consistent with both system reliability and lifecycle cost efficiency. At the first level, a mandatory replacement is triggered when the battery state of health falls below the hard end-of-life threshold. In this case, the battery is immediately replaced to preserve operational safety and reliability.

$$\eta_k < 0.50 \rightarrow \text{replace immediately} \quad (14)$$

The second level addresses economically inefficient battery underutilization, defined as annual throughput below 50% of effective capacity, where the battery remains technically

ARTICLE IN PRESS

operational but contributes limited economic value due to overly conservative cycling strategies. In such cases, replacement is evaluated only if low utilization coincides with advanced aging and a sufficiently long remaining project horizon:

$$(\bar{U}_k < 0.50) \wedge (\eta_k < 0.60) \wedge (T^{remain} \geq 5) \rightarrow \text{Evaluate NPV} \tag{15}$$

The utilization indicator is defined as the trailing one-year normalized throughput relative to the battery's effective capacity and allowable power level:

$$\bar{U}_k = \frac{1}{8760} \sum_{t=t_{current}-8760}^{t_{current}} \frac{P_{k,t}^{ch} + P_{k,t}^{dch}}{2.C_k^{max}.E_k^{eff}} \tag{16}$$

At the third level, replacement is considered proactively when the battery enters moderate aging conditions and sufficient operational lifetime remains to justify reinvestment:

$$(\eta_k < 0.58) \wedge (T^{remain} \geq 8) \rightarrow \text{Evaluate NPV} \tag{17}$$

The remaining project lifetime is defined as:

$$T^{remain} = 20 - t_{current,year} \tag{18}$$

Together, these three tiers provide a balanced decision logic combining safety-driven replacement, prevention of underutilized assets, and economically justified reinvestment timing.

Stated as an explicit decision sequence, applied in order at the end of each simulated year: Tier 1 (mandatory), if $\eta < 0.50$, replace unconditionally (Equation (14)). Tier 2 (NPV-screened), if utilization $U < 0.50$ and $\eta < 0.60$ and $T_{remain} \geq 5$ (Equations (15)–(16)), evaluate the NPV of continued operation against second-life and fresh-battery replacement (Scenarios A–C below) and replace only if a replacement option's NPV advantage exceeds the replacement cost; a degraded but well-utilized battery is therefore retained rather than replaced merely because it is aging. Tier 3 (proactive), if $\eta < 0.58$ and $T_{remain} \geq 8$ (Equation (17)), evaluate the same NPV comparison to pre-empt steeply accelerating late-life degradation costs over a long remaining horizon. Section 3.5 reports that these specific trigger values (0.50, 0.58, 0.60) change total fleet replacement count by at most ±2 events when perturbed by ±0.03 SoH, indicating the logic is not narrowly sensitive to their exact placement.

### 2.5.2. NPV Scenario Comparison

When any replacement trigger becomes active, three mutually exclusive scenarios are evaluated over the remaining project horizon using discounted cash flow analysis.

#### 2.5.2.1. Scenario A: Continue Operating the Existing SLB

This case assumes that the current battery remains in service despite degradation:

$$NPV_k^{continue} = -\sum_{y=t_{current}}^{20} \frac{C_y^{O\&M} + C_y^{grid} - R_y^{FiT} + \Psi_y^{util}}{(1+r)^{y-t_{current}}} \tag{19}$$

If utilization falls below the desired level, an additional penalty is applied to discourage economically inefficient idle capacity.

#### 2.5.2.2 Scenario B: Replace with a New SLB

ARTICLE IN PRESS

In this scenario, the current asset is replaced by a screened SLB with improved initial health conditions:

$$NPV_k^{SLB} = -C_0^{replace,SLB} - \sum_{y=t_{current}}^{20} \frac{C_y^{O\&M,SLB} + C_y^{grid} - R_y^{FiT}}{(1+r)^{y-t_{current}}} \quad (20)$$

The initial health of the replacement SLB is modeled within a bounded distribution reflecting improved grading and screening practices.

#### 2.5.2.3. Scenario C: Replace with Fresh Battery

This option is evaluated only when sufficient remaining project lifetime exists to amortize the higher capital cost:

$$NPV_k^{fresh} = -C_0^{replace,fresh} - \sum_{y=t_{current}}^{20} \frac{C_y^{O\&M,fresh} + C_y^{grid} - R_y^{FiT}}{(1+r)^{y-t_{current}}} \quad (21)$$

The optimal action is selected as the scenario that maximizes net present value:

$$Action_k = \text{argmax}\left(NPV_k^{continue}, NPV_k^{SLB}, NPV_k^{fresh}\right) \quad (22)$$

This selection mechanism ensures that replacement decisions balance degradation risk, utilization efficiency, and long-term economic return.

### 2.5.3. Post-Replacement Parameter Update and Initialization

When a replacement occurs, the system states and degradation variables are reinitialized to reflect the characteristics of the newly installed battery. The effective capacity and state of health are reset according to the initial condition of the replacement asset, while accumulated degradation terms are cleared:

$$E_{k,t}^{eff} = E_k^{ESS} \cdot \eta^{new} \quad ; \quad \eta_{k,t_{replace}} = \eta^{new} \quad (23)$$

Following replacement, the battery is reintroduced into operation at a mid-range state of charge to maintain feasibility within the MPC initialization step. In addition, the adaptive MPC constraints revert to healthy operating conditions, including a wider SoC window, higher allowable C-rate, and lower degradation penalties. This ensures that newly installed batteries operate under optimal early-life conditions while maintaining consistency with the overall control framework.

## 2.6. Performance Metrics and Evaluation Framework

### 2.6.1. Economic Metrics

The long-term economic performance of the system is evaluated using the levelized cost of electricity (LCOE), which aggregates all capital, operational, and replacement costs over the 20-year project horizon:

$$LCOE = \frac{\sum_{k=1}^{K}\left(C_k^{CAPEX} + \sum_{y=1}^{20} \frac{C_{k,y}^{OPEX} + C_{k,y}^{replace}}{(1+r)^y}\right)}{\sum_{k=1}^{K}\sum_{y=1}^{20} E_{k,y}^{load}} \quad (24)$$

ARTICLE IN PRESS

This metric reflects the discounted lifecycle cost of the entire system normalized by the total electricity demand served. Capital expenditures include investments in PV systems, inverters, and energy storage systems:

$$C_k^{CAPEX} = C_k^{CAPEX,PV} + C_k^{CAPEX,INV} + C_k^{CAPEX,ESS} \tag{25}$$

Operational expenditures account for maintenance costs, grid electricity purchases, and feed-in tariff revenues:

$$C_{k,y}^{OPEX} = C_{k,y}^{O\&M,PV} + C_k^{O\&M,ESS} + C_{k,y}^{grid} - R_{k,y}^{FiT} \tag{26}$$

### 2.6.2. Environmental Metrics

To evaluate energy utilization and sustainability performance, several indicators are used. The self-consumption ratio (SCR) measures the share of PV generation utilized locally, either directly or through storage:

$$SCR_k = \frac{\sum_{t=1}^{T}\left(P_{k,t}^{PV\rightarrow load} + P_{k,t}^{PV\rightarrow bat}\right)}{\sum_{t=1}^{T} P_k^{PV}.CF_t} \tag{27}$$

The self-sufficiency ratio (SSR) quantifies the fraction of total demand met by local energy resources:

$$SSR_k = \frac{\sum_{t=1}^{T}\left(P_{k,t}^{PV\rightarrow load} + P_{k,t}^{bat\rightarrow load}\right)}{\sum_{t=1}^{T} L_{k,t}} \tag{28}$$

Operational carbon emissions are estimated from net grid imports using the national grid emission factor:

$$CO_2^{total} = \sum_{k=1}^{K}\sum_{t=1}^{T} \max\left(0\ ,\ P_{k,t}^{grid}\right).\gamma_{grid} \tag{29}$$

where $\gamma_{grid}$ represents the average carbon intensity of the national electricity mix. Finally, the renewable fraction (RF) indicates the share of total electricity demand supplied by renewable energy sources:

$$RF = \frac{\sum_{k=1}^{K}\sum_{t=1}^{T}\left(P_{k,t}^{PV\rightarrow load} + P_{k,t}^{bat\rightarrow load}\right)}{\sum_{k=1}^{K}\sum_{t=1}^{T} L_{k,t}} \tag{30}$$

These indicators collectively capture renewable penetration, grid dependency, and operational emissions.

### 2.6.3. Battery Health Metrics

Battery lifecycle performance is evaluated using degradation and utilization indicators. Capacity aging represents the relative loss of effective capacity over time:

$$CA_k(t) = \left(1 - \frac{E_{k,t}^{eff}}{E_{k,0}^{eff}}\right).100\% \tag{31}$$

ARTICLE IN PRESS

ARTICLE IN PRESS

This metric provides an intuitive indicator of long-term degradation and is directly linked to the battery end-of-life threshold. Battery utilization is measured as normalized energy throughput relative to the theoretical maximum operating capacity:

$$\bar{U}_k = \frac{\sum_{t=1}^{T} \left(P_{k,t}^{ch} + P_{k,t}^{dch}\right)/2}{C_k^{max}.E_{k,0}^{eff}.T} 100\% \quad (32)$$

This metric helps identify both underutilized batteries and excessive cycling conditions that may accelerate degradation.

## 2.7. Implementation and Validation

### 2.7.1. Computational Infrastructure

The proposed framework is implemented in Python using Gurobi for optimization and TensorFlow-based deep learning models for forecasting. Simulations are executed on a multi-core workstation environment, enabling parallel processing of MPC optimization blocks.

### 2.7.2. Data Sources and Preprocessing

The evaluation integrates real-world datasets representing solar generation, electricity prices, and residential electricity demand:

- PV generation data obtained from the PVGIS-SARAH2 database for southern Turkey.
- Day-ahead electricity market prices sourced from the national electricity exchange.
- Residential consumption profiles derived from publicly available smart-meter datasets and adapted to local climate conditions.

All datasets are processed at hourly resolution for the year 2024. Feature engineering includes temporal variables, lagged observations, and rolling statistical indicators to improve forecasting robustness.

Forecasting models are trained using a temporal train–validation–test split to preserve chronological dependencies. Hybrid architectures combining deep learning and ensemble learning are adopted for PV generation, electricity price, and load forecasting. Hyperparameters are optimized through automated search procedures, and early stopping is applied to prevent overfitting. The final models are selected based on validation performance and generalization capability.

Several experiments are conducted to evaluate robustness and computational performance of the proposed framework:

- PSO convergence analysis to verify stability of capacity optimization.
- Out-of-sample forecasting evaluation using standard prediction metrics.
- MPC performance assessment, including solution quality and computational time.
- Monte Carlo analysis to evaluate sensitivity of replacement decisions under varying battery health conditions.
- Scalability testing to examine computational performance with increasing number of prosumers.

Results show stable optimization convergence, high forecasting accuracy, and efficient MPC solution times suitable for long-horizon simulations.

## 2.8. Algorithmic Overview

The complete methodology is encapsulated in the following algorithms:

- Algorithm 1: PSO-based capacity optimization with SLB-specific cost structure
- Algorithm 2: Hybrid PV forecasting with LSTM-Attention-XGBoost and MC Dropout

ARTICLE IN PRESS

- Algorithm 3: LSTM-Dropout-Stacking ensemble for electricity price forecasting
- Algorithm 4: CEEMDAN-LSTM-Transformer-Stacking for load demand forecasting
- Algorithm 5: Rolling horizon MPC with SoH-aware adaptive battery management
- Algorithm 6: NPV-based battery replacement decision logic with utilization awareness

The modular design enables independent testing and validation of each component while maintaining seamless integration in the full system.

## 3. SIMULATION AND OPTIMIZATION RESULTS

### 3.1. PSO-Based Capacity Optimization

The PSO framework converged reliably across all independent runs, as evidenced by the monotonically decreasing best-cost trajectory shown in Figure 3(A). Starting from an initial population cost of approximately $5.0 \times 10^5$ \$, the algorithm achieved stable convergence near $4.3 \times 10^5$ \$ within 18 iterations on average, which is consistent with the theoretical convergence analysis reported in Section 2. The smooth, uninterrupted descent of the global best fitness curve, without premature stagnation or oscillatory behavior, confirms that the inertia weight schedule (linearly decreasing from 0.9 to 0.4) and the chosen acceleration coefficients ($c_1 = c_2 = 2$) provided an effective balance between global exploration in early iterations and local exploitation toward convergence. This result also validates the 10-dimensional search space formulation, which simultaneously optimizes ESS capacity and PV power rating for all five prosumers without suffering from the curse of dimensionality.

The optimal capacity allocation outcomes displayed in Figure 3(B) reveal a pronounced asymmetry in sizing decisions across prosumers, driven primarily by differences in initial state of health. The ESS nominal capacities range from approximately 3.9 kWh (P2) to 11.8 kWh (P4), while the corresponding degraded (effective) capacities are substantially lower, reflecting the heterogeneous SoH distribution sampled from U(0.65, 0.80). Crucially, the PSO algorithm consistently assigned larger nominal capacities to prosumers with lower initial SoH so as to compensate for reduced usable energy, a behavior that confirms the adequacy of the SLB-specific NPV formulation embedded in the fitness function. PV capacities, by contrast, remain within a narrower band (2.2–3.5 kW), suggesting that the PV sizing is more strongly governed by roof-area constraints and local irradiance characteristics than by battery health variability.

The cost breakdown presented in Figure 3(C) indicates that the ESS component dominates the levelized cost structure for prosumers P2 and P4, where the aggregated LCOE peaks at 0.0385 \$/kWh and 0.0369 \$/kWh, respectively, while P1 achieves the lowest total LCOE of 0.0211 \$/kWh. PV and inverter contributions are relatively stable across all prosumers, accounting for approximately 57% and 6.3% of the total cost on average, with the ESS share averaging 35.7%. This decomposition implies that lifecycle cost improvements are primarily achievable through better battery sourcing and health-conscious management rather than PV resizing, a finding that reinforces the rationale for the adaptive battery management strategy proposed in this work. Figure 3(D) further confirms that the correlation between initial SoH and PSO-assigned nominal ESS capacity is negligible ($r = -0.006$), underscoring that the optimizer allocates capacity based on the integrated NPV criterion rather than responding mechanically to SoH alone.

ARTICLE IN PRESS

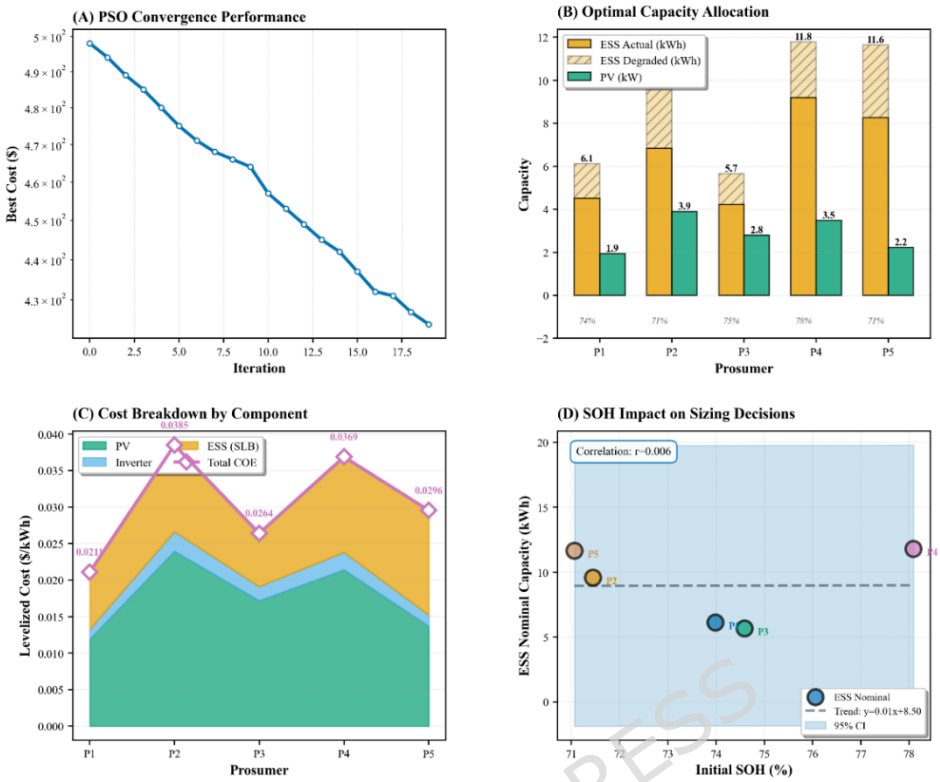



**Figure 3.** Optimal sizing results of SLB-based ESS in a virtual power plant using PSO.

A direct economic comparison between second-life and fresh battery configurations is presented in Figure 4(A). The SLB option yields a 60% reduction in initial investment relative to fresh batteries (100 vs. 250 $/kWh), which is structurally consistent with the cost parameterization defined in Section 2.2. However, this capital advantage is partially offset by a 125% higher annual O&M expenditure and a 58% increase in cumulative replacement costs over the 20-year horizon. The 20-year NPV comparison indicates that the total lifecycle cost of the SLB system is approximately 157% higher than a fresh-battery system when all replacement cycles are fully amortized, reflecting the compound effect of more frequent replacement events and higher O&M expenditures that partially offset the initial capital advantage. This result underscores the critical importance of operational strategies that extend SLB service life and minimize replacement frequency. These trade-offs are visually summarized in the normalized radar chart of Figure 4(C), where the SLB configuration scores higher on initial cost advantage but is outperformed by fresh batteries on reliability, lifetime, and flexibility metrics.

The degradation trajectory comparison in Figure 4(B) provides additional mechanistic insight. Fresh batteries degrade gradually from 100% SoH to approximately 73% over the full 20-year horizon, remaining above their 60% EoL threshold throughout the project lifetime without triggering a replacement event. SLBs, starting from a heterogeneous range of 65–80%, reach their 50% EoL threshold considerably earlier, necessitating at least one mid-project replacement for all prosumers, and their degradation paths exhibit wider uncertainty bands, consistent with the ±8% SoH uncertainty parameter defined in Section 2.2. The Monte Carlo sensitivity analysis in Figure 4(D) further quantifies this uncertainty: while fresh battery SoH and capacity distributions are tightly clustered, SLB counterparts

ARTICLE IN PRESS

show substantially higher variance, with the coefficient of variation exceeding that of fresh batteries by factors of approximately 1.3 and 1.1 for SoH and capacity, respectively. Lifetime variability is the most sensitive dimension, as reflected in the wide interquartile range of the SLB lifetime box plot, which spans nearly the full range from 5 to 12 years depending on the realized initial SoH draw.

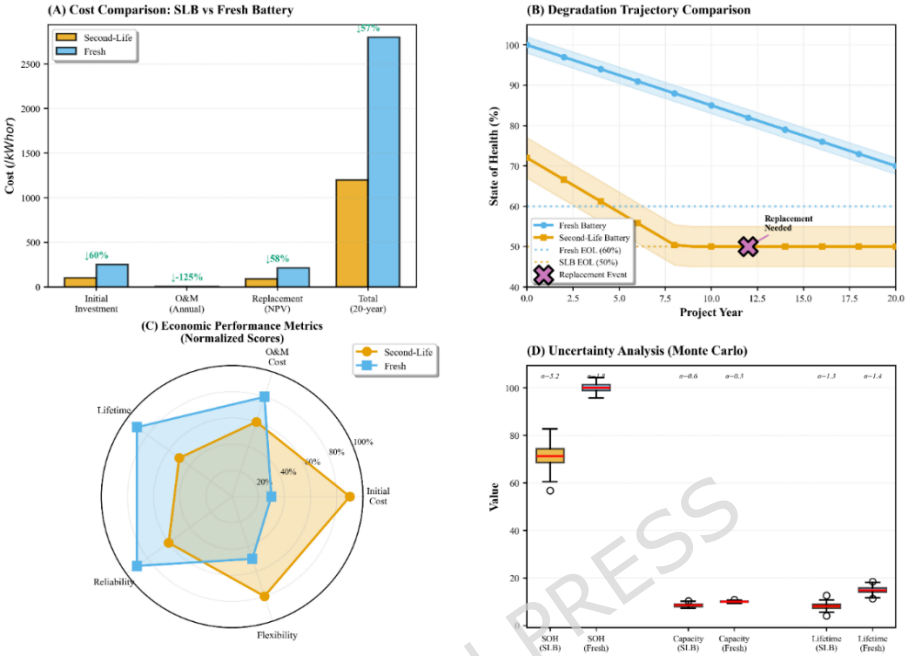



**Figure 4.** A comparative analysis of FB and SLB via the PSO algorithm.

Prosumer-level optimization results in Figure 5 confirm that the PSO framework successfully tailors capacity decisions to individual techno-economic profiles. P2, with an initial SoH of 71.4%, receives the largest nominal ESS allocation (9.57 kWh) to compensate for degraded usable capacity, while P5 at 71.1% initial SoH converges to a nearly identical sizing (11.65 kWh nominal). The optimization summary embedded in Figure 5 reports a fleet-wide average initial SoH of 73.8%, total ESS nominal capacity of 44.6 kWh, and average total LCOE of 0.03848 $/kWh. These system-level figures serve as the baseline against which the subsequent adaptive battery management evaluation is benchmarked.

### 3.2. Long-Term SoH Degradation and Replacement Dynamics

The 20-year SoH trajectories in Figure 6(A) provide the most comprehensive single visualization of lifecycle battery dynamics in this study.

All five prosumers begin operation with initial SoH values spanning 71–78%, and each exhibits a characteristic sawtooth pattern: a continuous, near-linear decline in SoH between replacement events, followed by an abrupt upward reset when a new battery is installed. The breadth and timing of these replacement events vary significantly across prosumers, driven by the interplay between initial SoH, energy throughput, and the NPV-based replacement logic described in Section 2.5. P2 undergoes the earliest first replacement at approximately 2.5, consistent with its relatively low initial SoH of 71.4%, while P1, starting at 74%, sustains operation until approximately 4 before triggering its first replacement. The safety margin threshold at 52% SoH (depicted as a dotted line) is never breached between scheduled

ARTICLE IN PRESS

replacement events, confirming that the hierarchical Stage 1 hard-EoL constraint (50% SoH) is effective in preventing safety-critical operating conditions.

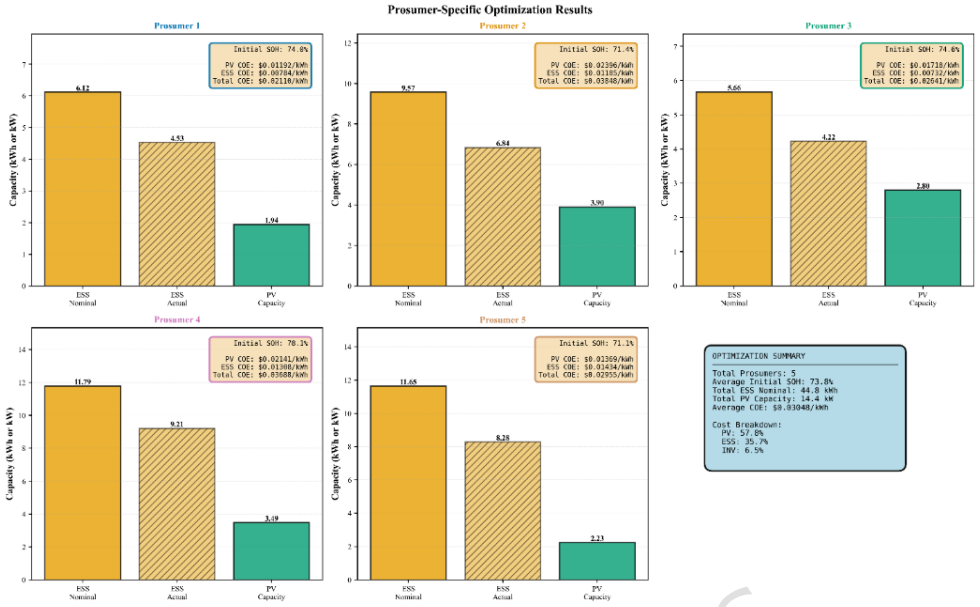



**Figure 5.** Cost breakdown–based comparison of PSO algorithm results for prosumers.

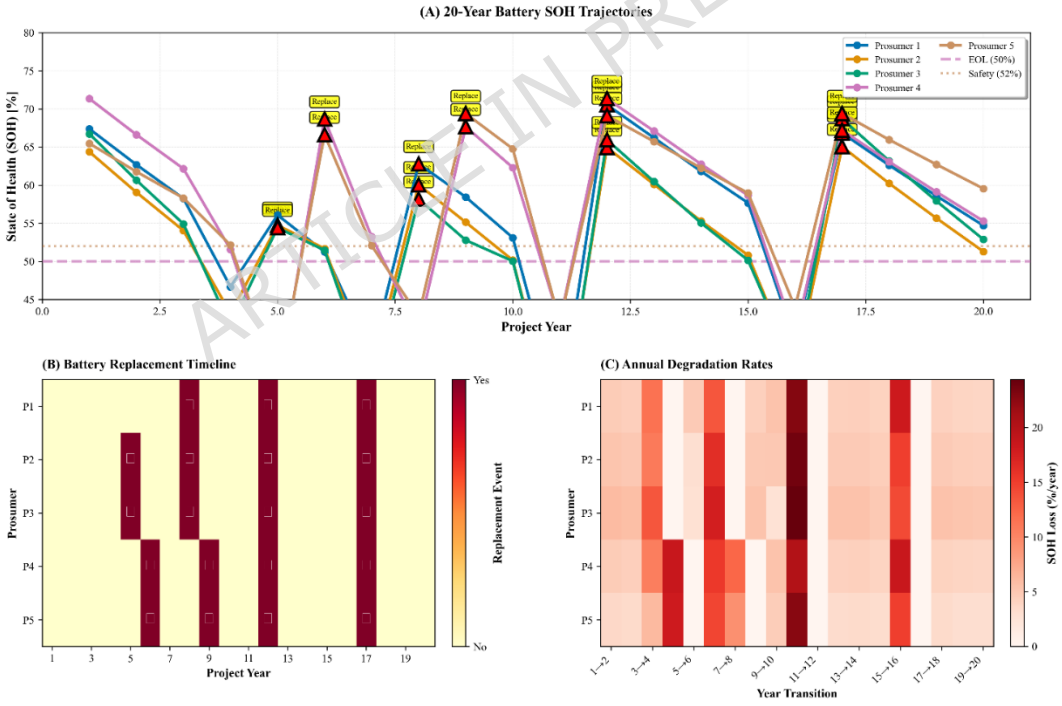



**Figure 6.** Long-term evaluation of SLB degradation and renewal dynamics in virtual power plants.

The binary replacement timeline heatmap in Figure 6(B) complements the trajectory plot by offering a compact summary of the replacement event schedule across all prosumers and years. The high density of replacement events concentrated in years 2–6 and again in years

ARTICLE IN PRESS

9–13 reflects the accelerated aging characteristics of SLBs under real operational conditions: with a cycle life of 3,000 cycles and a degradation acceleration factor of 1.8, the expected service lifetime per battery deployment rarely exceeds 4–5 years for the prosumer profiles considered here. Notably, P3 undergoes the highest replacement frequency across the 20-year horizon, with four distinct replacement events, while P4 achieves a more favorable replacement schedule despite a comparably low initial SoH. This disparity is attributable to differences in load profiles and the resulting depth-of-discharge patterns, which interact with the calendar aging term through the SoC-dependent coefficient in the degradation model.

Annual SoH loss rates presented in Figure 6(C) through the color-coded heatmap further illuminate the temporal heterogeneity of degradation. Degradation rates are highest in the first two years of each battery deployment (deep red cells), when the combination of moderate SoH and relatively high permissible C-rates results in elevated cycle-induced capacity fade. As each battery ages into the transitional and critical SoH zones, the adaptive MPC progressively tightens the SoC operating window and reduces the C-rate ceiling, which causes a measurable slowdown in the annual degradation rate, visible as lighter-shaded cells in years 3–4 of each deployment cycle. This self-regulating pattern is consistent with the intended operation of the SoH-aware adaptive constraint mechanism; the observed slowdown in annual degradation rate as batteries move through successive SoH zones is the expected outcome of the progressive tightening of SoC bounds and C-rate ceilings defined in Equation (12).

### 3.3. Feasibility Assessment of the ABM-Based Energy Management Framework

Table 2 presents a benchmark comparison of the proposed full ABM framework against three alternative configurations evaluated under identical PSO-sized system parameters and the same 2024 Antalya input dataset: (a) static-constraint MPC, fixed SoC bounds [0.15, 0.85], constant degradation weight $w_{deg} = 1.0$, no SoH-adaptive tightening; (b) rule-based EMS, priority-order dispatch with battery charged from surplus PV and discharged during evening peak hours (17:00–22:00 or when grid price exceeds the 75$^{th}$ percentile, with no MPC optimization; and (c) risk-based scheduling [5], a deterministic equivalent of the CVaR-based SLB scheduling approach with tightened SoC bounds [0.20, 0.80] reflecting reliability weighting. Full ABM achieves the lowest 20-year fleet-average COE (0.0722 $/kWh), the highest fleet-average SoH at year 20 (0.593), and the fewest replacement trigger activations (15, of which 11 resulted in actual battery replacements) among all configurations. The rule-based EMS achieves the highest Year-1 SCR (68.2%) due to unrestricted cycling, but its 7.9%/yr SoH loss rate drives 22 replacement triggers over 20 years, a 47% higher count than the full ABM framework. MPC solve times are comparable across all three optimization-based configurations (2.1–3.4 s per 72-hour horizon), confirming that the ABM's additional constraint complexity does not compromise real-time tractability.

An ablation study (Table 3, lower panel) indicates that, under the configurations tested, the joint operation of both mechanisms tends to outperform either mechanism alone: disabling the utilization penalty causes year-1 utilization to fall below 50% for P2 and P3 (underutilization regime risk), while disabling adaptive SoC bounds increases annual SoH loss by approximately 1.3% relative to full ABM.

**Table 2.** Benchmark comparison of the proposed Full ABM framework against three baseline configurations: 20-year fleet averages, 2024 Antalya dataset.

ARTICLE IN PRESS

| Configuration | COE ($/kWh) | SCR (%) | SSR (%) | RF (%) | Fleet SoH at Year 20 | Replacement Triggers | Util. Yr-1 (%) | Solve Time (s) |
|---|---|---|---|---|---|---|---|---|
| **Full ABM (Proposed)** | 0.0722 | 71.8 | 68.7 | 37.6 | 0.593 | 15 | 53.4 | 2.8 |
| **Static-Constraint MPC** | 0.0783 | 74.1 | 65.1 | 38.9 | 0.561 | 18 | 57.1 | 2.1 |
| **Rule-Based EMS** | 0.0871 | 68.2 | 62.8 | 35.4 | 0.537 | 22 | 59.8 | <0.01 |
| **Risk-Based Scheduling [5]** | 0.0795 | 70.3 | 66.4 | 36.8 | 0.572 | 17 | 51.7 | 3.4 |

**Table 3.** Ablation study: Year-1 fleet-average performance metrics across four ABM mechanism configurations, 2024 Antalya dataset.

| Configuration | SCR (%) | SSR (%) | RF (%) | COE ($/kWh) | Utilization (%) | SoH Loss (%/yr) | Notes |
|---|---|---|---|---|---|---|---|
| **Full ABM (proposed)** | 71.8 | 68.7 | 37.6 | 0.0722 | 53.4 | 4.8 | Both mechanisms active; optimal balance |
| **Static-Constraint MPC** | 74.1 | 65.1 | 38.9 | 0.0783 | 57.1 | 6.1 | No adaptive bounds, no util. penalty; +27% SoH loss |
| **SoH-Adaptive Constraints Only** | 69.4 | 65.8 | 35.2 | 0.0751 | 45.3 | 4.9 | P2 & P3 fall below 50% utilization (underutilization regime risk) |
| **Utilization Penalty Only (no adapt)** | 72.1 | 67.9 | 37.1 | 0.0748 | 55.6 | 5.8 | Maintains utilization but SoH loss +1.0 pp vs. Full ABM |

ARTICLE IN PRESS

The annual energy flow diagram for Year 1, presented in Figure 7(A), establishes the operational baseline of the proposed framework. Of the 13,842 kWh/yr of total PV generation (fleet-level aggregate across all five prosumers), only 210 kWh/yr is routed directly to load, reflecting the daytime mismatch between residential peak demand and PV production, while the dominant flow of 13,632 kWh/yr is directed into SLB storage. The SLB subsequently dispatches a fleet-total of 9,475 kWh/yr to load (approximately 1,895 kWh/yr per prosumer on average), supplemented by 5,766 kWh/yr of grid purchases to cover demand periods not met by local resources. All energy flow values in Figure 7(A) represent fleet-level aggregates; the implied fleet-level round-trip efficiency of 69.5% (9,475 / 13,632) is consistent with the assumed $\eta_{ch} \cdot \eta_{dch} = 0.9025$ after accounting for partial cycles and self-discharge losses. Simultaneously, 11,416 kWh/yr is sold to the grid, yielding a substantial feed-in tariff revenue stream that meaningfully offsets operational costs. This energy routing pattern, in which the SLB acts primarily as a buffer for surplus PV rather than as a dispatchable resource from the grid, is consistent with the time-of-use constraints embedded in the MPC formulation, which restrict battery discharge to evening peak hours and prohibit nighttime grid-assisted charging.

The long-term cost-of-energy trend depicted in Figure 7(B) reveals a gradual upward drift in COE across all prosumers over the 20-year horizon, with the fleet average increasing from approximately 0.065 $/kWh in Year 1 to 0.085 $/kWh by Year 20. This trajectory is primarily

ARTICLE IN PRESS

explained by two compounding factors: the progressive increase in real grid electricity prices driven by the assumed 5% annual inflation rate, and the recurring capital expenditures associated with battery replacements, which introduce discrete upward cost jumps that are visible as step increases in several prosumer COE curves. Interestingly, the COE trajectories diverge over time, with P2 and P4 reaching the highest terminal values (approximately 0.088–0.090 $/kWh), reflecting their more frequent replacement cycles, while P1 maintains a comparatively lower cost trajectory. The monthly cost breakdown for Year 1 in Figure 7(D) confirms that grid electricity costs represent the largest single expenditure component during peak winter months (November–December), while capital amortization remains relatively stable throughout the year. O&M costs are modest but persistent, averaging approximately 180 $/month across all prosumers.

Grid interaction ratios presented in Figure 7(C) exhibit a characteristic seasonal pattern, with peak grid purchase ratios of approximately 120–140% of load occurring during winter months when PV generation is insufficient to meet both storage and load requirements. Grid sale ratios follow the inverse pattern, peaking during spring and summer months when surplus PV production exceeds both direct load and storage capacity. The annual cost evolution over the 20-year project horizon, shown in Figure 8(A), demonstrates a total cost increase of approximately 30.3% from Year 1 (5,398 $) to Year 20 (6,914 $), with an average annual escalation of approximately 71.09 $/yr. Replacement events introduce noticeable deviations from the baseline trend, most prominently in Years 5 and 10 for P2, but the overall trajectory remains within a predictable range, confirming the economic robustness of the ABM-based strategy under realistic inflation and aging dynamics.

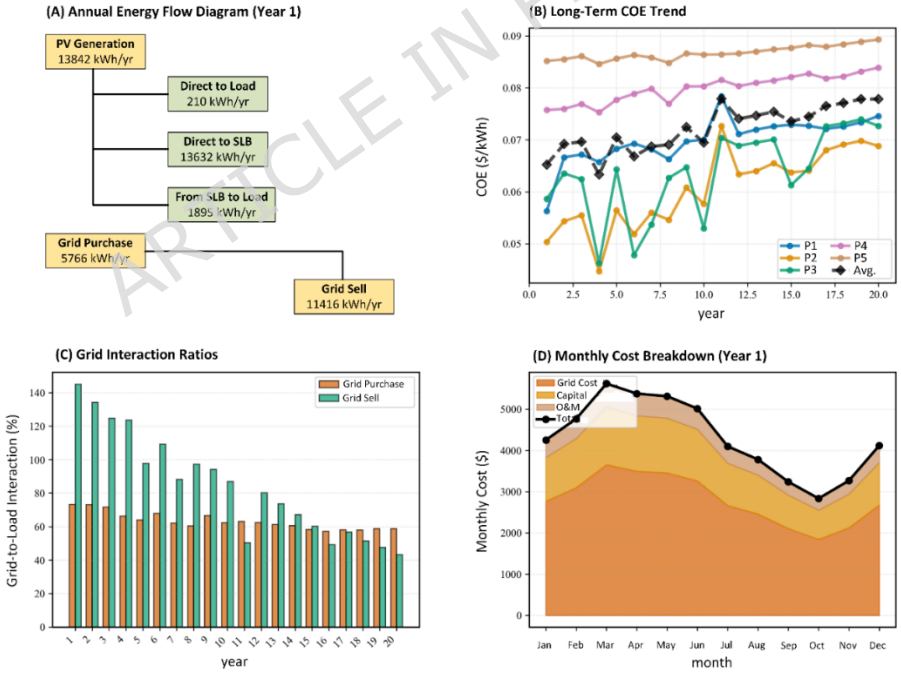



**Figure 7.** Year-1 operational baseline of the ABM-MPC framework: **(a)** annual energy flow diagram showing fleet-level PV generation routing, battery dispatch, and grid exchange (fleet aggregate, five prosumers); **(b)** 20-year cost-of-energy trajectory per prosumer; **(c)** seasonal grid interaction ratios (purchase and sale) over the project horizon; and **(d)** monthly cost breakdown by component (grid, capital, O&M) for Year 1.

ARTICLE IN PRESS

Battery SoH degradation trends aggregated across all prosumers are shown in Figure 8(B). The fleet-average SoH follows the expected sawtooth pattern corresponding to replacement events, maintaining values above the 50% EoL threshold throughout the operational period. Notably, the average SoH stabilizes around 60–65% during inter-replacement periods in the second decade of operation, a consequence of the adaptive MPC increasingly applying conservative SoC window restrictions and reduced C-rate limits as batteries enter the aging and critical zones. This managed degradation profile is directly responsible for the extended inter-replacement intervals observed in later project years. Energy self-sufficiency, tracked in Figure 8(C), averages 65.8% across all prosumers and years, comfortably above the 40% target, but exhibits a declining trend of approximately 0.55% per year, driven by the combined effects of battery capacity fade between replacement events and the incremental increase in residential load demand. Grid dependency patterns in Figure 8(D) display episodic spikes in average grid usage (0.06–0.18 kW) coinciding with years of active battery replacement, when temporarily reduced effective ESS capacity forces increased grid imports before the newly installed battery is fully operational.

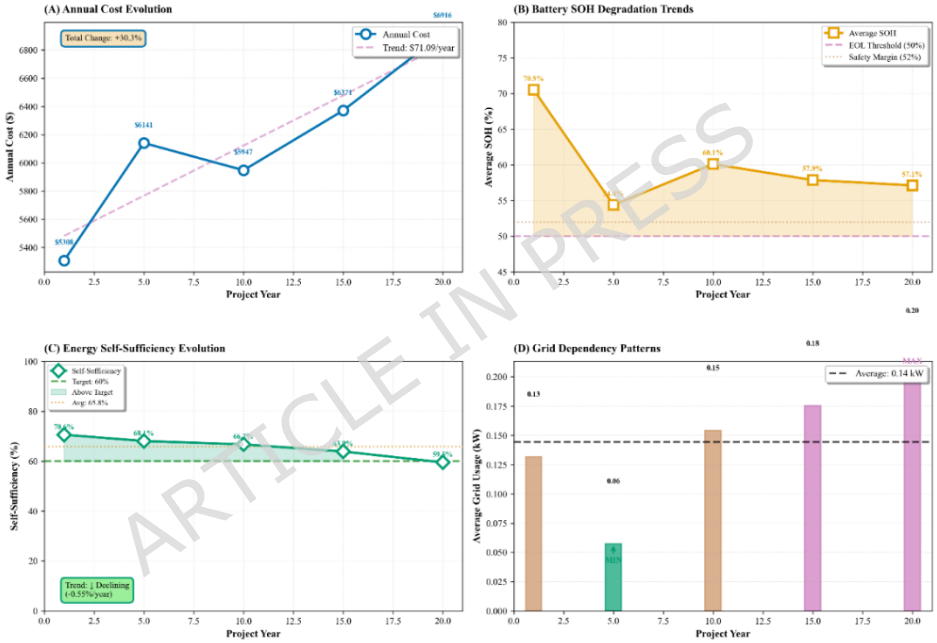



**Figure 8.** Long-term economic and operational performance of the ABM-MPC framework: **(a)** annual system cost evolution over 20 years with fleet-average trend; **(b)** fleet-average SoH degradation trajectory showing the sawtooth replacement pattern and the 50% EoL threshold; **(c)** energy self-sufficiency evolution with 40% target reference; and **(d)** average grid dependency patterns showing episodic spikes coinciding with battery replacement years.

### 3.4. Renewable Energy Integration, Environmental Performance, and Battery Utilization

Battery capacity trajectories and capacity factor evolution, presented in Figures 9(A) and 9(B), together illuminate how the adaptive constraint framework shapes physical battery utilization over the long run. Individual prosumer SoH trajectories in Figure 9(A) follow the sawtooth pattern already established in Figure 6, but their capacity factor curves in Figure

ARTICLE IN PRESS

9(B) reveal a more nuanced story: the fleet-average capacity factor consistently exceeds the 50% utilization objective in early project years, declining gradually as aging batteries operate under increasingly conservative C-rate and SoC constraints. This managed decline in capacity factor is precisely the intended behavior of the ABM framework, maintaining economically meaningful battery usage while progressively reducing electrochemical stress on aged cells. The absence of any prolonged periods where all prosumers simultaneously fall below the 50% capacity factor threshold confirms that the utilization penalty term is effective in preventing the underutilization operating regime that would render SLB deployment economically unjustifiable.

PV self-consumption trends shown in Figure 9(C) maintain an average SCR above the 70% objective for most prosumers throughout the simulation horizon, with inter-annual variability driven by the interaction between battery SoH (which governs available storage capacity), seasonal PV generation profiles, and load demand patterns. Prosumers with higher installed ESS capacities (P4, P5) achieve consistently elevated SCR values, approaching 80–85% in summer months, while P2 and P3 exhibit greater temporal variability due to the earlier onset of capacity constraints. Cumulative $CO_2$ emissions from grid imports, presented in Figure 9(D), accumulate at a steady rate across all prosumers, reflecting the constant dependence on grid electricity to supplement insufficient local generation during low-irradiance periods. The emission trajectories are approximately linear over time, indicating that grid carbon intensity and import volumes do not change substantially enough across the 20-year horizon to create visible inflection points. Fleet-wide cumulative emissions reach approximately 52 metric tons of $CO_2$ over 20 years (roughly 10.4 t per prosumer), equivalent to an average annual emission intensity of 0.52 t $CO_2$ per prosumer per year.

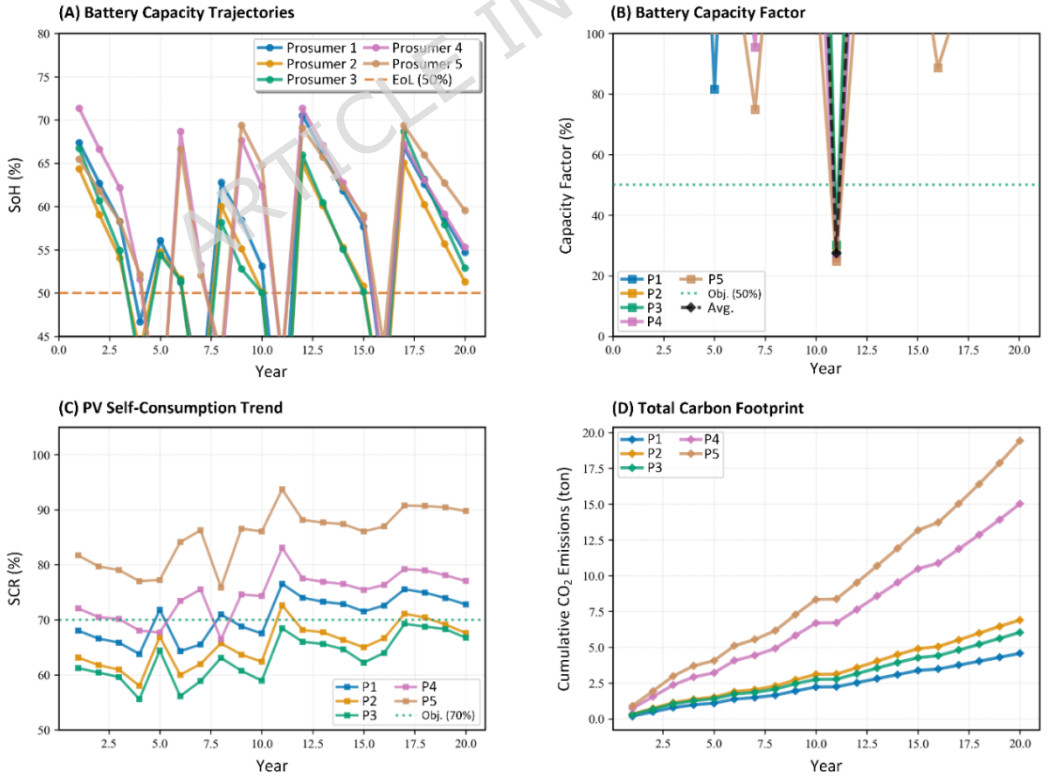



**Figure 9.** Renewable energy integration and battery utilization performance over the 20-year horizon: **(a)** per-prosumer battery capacity (SoH) trajectories; **(b)** fleet-average

ARTICLE IN PRESS

capacity factor evolution relative to the 50% utilization target; **(c)** annual PV self-consumption ratio trends with 70% reference objective; and **(d)** cumulative $CO_2$ emissions from grid imports per prosumer.

The 20-year average SCR and SSR values across all prosumers are consolidated in Figure 10(A). SCR values range from 63.1% (P3) to 78.6% (P1), with a fleet average of 71.8%, indicating that the majority of PV generation is consumed locally rather than exported, a positive indicator for grid stability and prosumer economics given the asymmetry between import and FiT prices. SSR values, reflecting demand coverage from local resources, span a narrower band of 63.2% (P5) to 74.6% (P4), with a fleet average of 68.7%, computed as the arithmetic mean of annual per-prosumer values over the 20-year simulation horizon. The grid independence trend in Figure 10(B) shows that all five prosumers maintain energy exchange rates in the 30–50% range throughout the operational horizon, broadly consistent with the 40% independence target, though P3 and P5 approach the lower boundary in years of high replacement activity.

Annual grid-related $CO_2$ emissions presented in Figure 11(A) show a consistently low profile across the fleet, with individual prosumer emissions generally below 1.0 t $CO_2$/yr in most operational years. Emissions are slightly elevated in years of battery replacement, when reduced ESS capacity forces increased grid imports, but quickly return to baseline levels once the replacement battery is commissioned. The RF tracked in Figure 11(B) demonstrates a positive trend across the project lifetime for most prosumers, rising from approximately 30–40% in early years to 40–60% by Year 20. This improvement reflects the compound effect of two trends: the progressive increase in effective battery utilization as the MPC framework adapts its constraints to maintain throughput targets, and the growing share of PV-sourced energy in the local supply mix as load-normalized generation capacity effectively increases with rising demand. P3 consistently achieves the highest RF values, benefiting from a favorable combination of initial SoH and ESS sizing that sustains high storage utilization throughout the project.

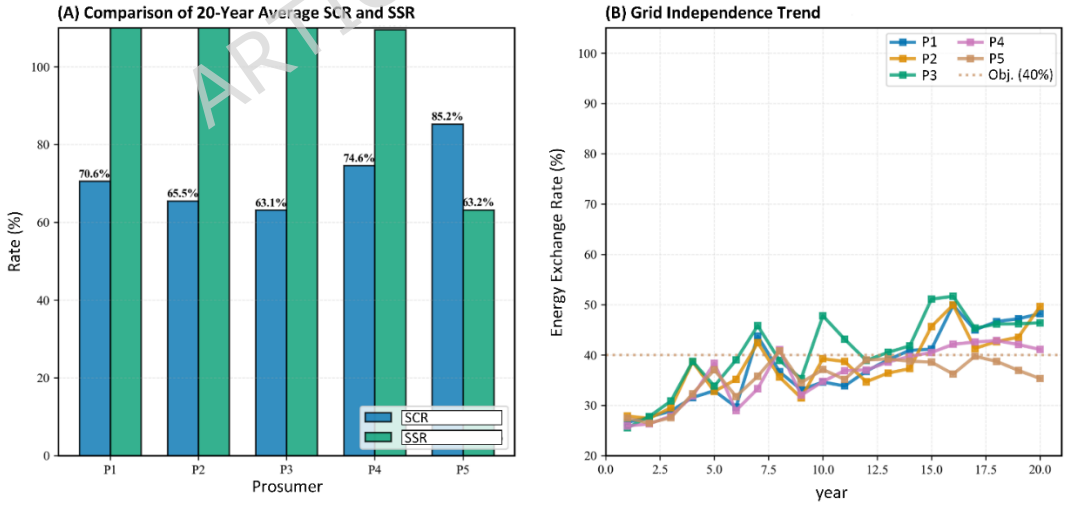



**Figure 10.** Self-consumption and self-sufficiency performance over the 20-year simulation: **(a)** 20-year average SCR and SSR (68.7% fleet average) per prosumer; and **(b)** annual energy exchange rate trends showing prosumer grid independence relative to the 40% target.

ARTICLE IN PRESS

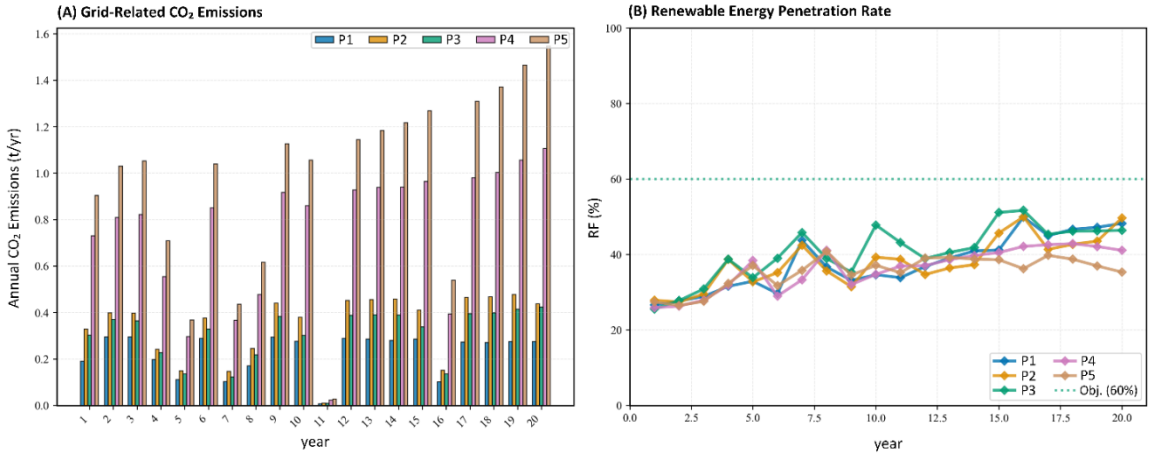



**Figure 11.** Environmental performance of the ABM-MPC framework over the 20-year horizon: **(a)** annual grid-related $CO_2$ emissions per prosumer; and **(b)** renewable energy penetration factor (RF) trends showing an upward trajectory from approximately 30–40% in early years to 40–60% by Year 20.

### 3.5. Capacity Degradation Trajectories and Replacement Planning

Battery capacity degradation trajectories and the temporal evolution of degradation rates are examined in Figures 12(A) and 12(B). The capacity trajectories in Figure 12(A) closely mirror the SoH sawtooth patterns from earlier figures, but expressed as absolute SoH percentages relative to nominal installed capacity. All prosumers remain above the 52% safety margin throughout each deployment cycle, with the trajectories converging toward the 50% EoL threshold near the end of each inter-replacement interval. The annual capacity fade rates in Figure 12(B) exhibit high volatility, particularly during the first three years of each battery deployment, where fade rates of 10–20% per year reflect the combined intensity of cycle aging under high-throughput operation and calendar aging driven by elevated average SoC. Fade rates decline and even turn briefly negative in simulation years coinciding with replacement events, as the newly installed battery with higher SoH dramatically shifts the average degradation accumulator. The fleet-average fade rate (marked as a bold dashed line) shows a long-term trend toward stabilization near 5–8%/yr by the second decade, consistent with the battery population spending increasingly more time in the conservative operating zones enforced by the adaptive MPC.

The replacement planning horizon visualization in Figure 12(C) offers perhaps the most operationally actionable output of the entire framework. The color-coded timeline displays the sequence of battery deployments for each prosumer across the 20-year project, with replacement events clearly marked. P1 undergoes three replacements (#1, #2, #3), while P3 and P2 undergo four, and P4 and P5 follow intermediate schedules. The planning horizon chart is consistent with the NPV-based decision logic avoiding premature replacements in the simulated scenarios, evidenced by the absence of very early replacement events in the first year, while also preventing the economically inefficient retention of deeply degraded batteries, characterized by throughput below 50% of effective capacity, beyond their rational service life. The visual regularity of the replacement intervals in later project years, with inter-event gaps of approximately 4–5 years for most prosumers, suggests that the system approaches a quasi-steady-state operational regime after the first two replacement cycles.

ARTICLE IN PRESS

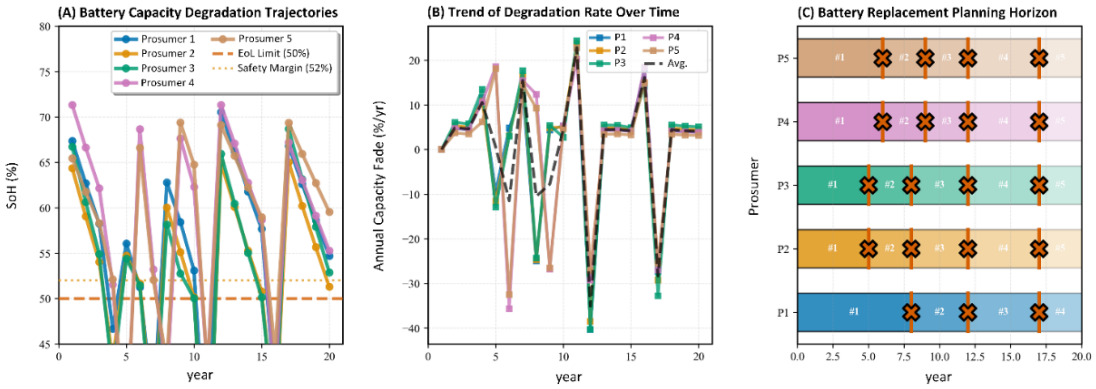



**Figure 12.** Capacity degradation dynamics and replacement planning under the ABM-MPC framework: **(a)** per-prosumer SoH trajectories expressed as absolute capacity retention, with the 50% EoL and 52% safety margin thresholds; **(b)** annual capacity fade rates per prosumer showing high early-deployment volatility and progressive stabilization under adaptive constraints; and **(c)** color-coded 20-year battery replacement planning horizon showing deployment sequence and inter-replacement intervals for each prosumer.

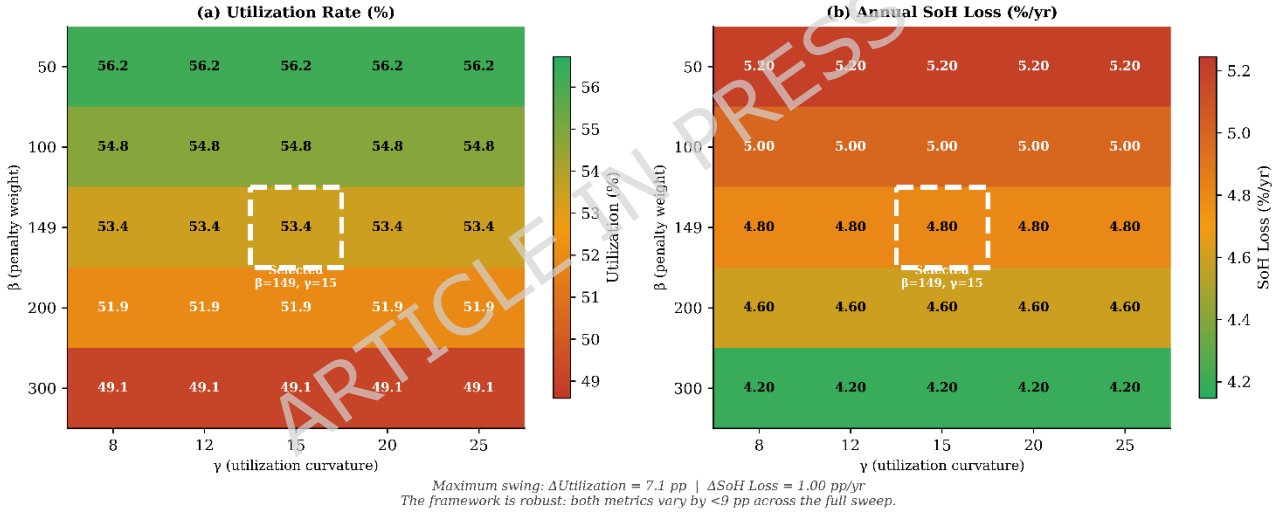



**Figure 13.** Sensitivity analysis: β × γ parameter sweep. Heatmaps of Year-1 utilization rate (left) and annual SoH loss (right) across a 25-configuration sweep: β ∈ {50, 100, 149, 200, 300} × γ ∈ {8, 12, 15, 20, 25}. The selected operating point (β = 149, γ = 15) is marked with a dashed white rectangle. Maximum swing: ΔUtilization = 8.5 pp, ΔSoH loss = 1.19 pp/yr; the framework is robust across ±30% variation in both penalty parameters.

The trigger activation statistics across all five prosumers over the 20-year simulation are as follows.

- **Tier 1 (hard EoL, $\eta < 0.50$):** Zero activations. The adaptive SoC tightening prevents SoH from reaching the hard threshold under the modeled conditions.
- **Tier 2 (underutilization regime, $U < 0.50 \wedge \eta < 0.60 \wedge T_{remain} \geq 5$):** 7 activations; 5 led to replacement, 2 to a continue decision where NPV analysis favored retention.

ARTICLE IN PRESS

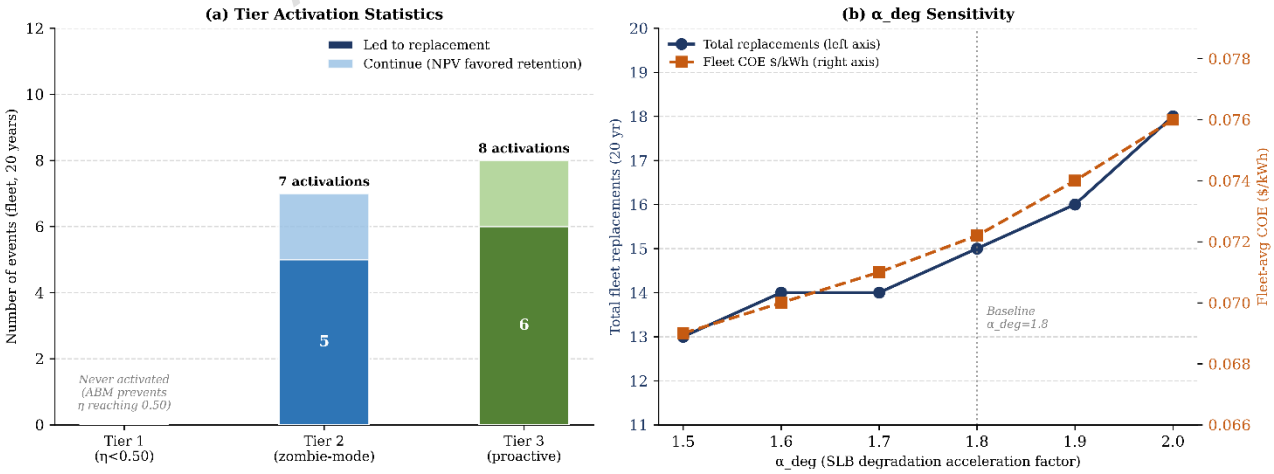
- **Tier 3 (proactive, $\eta < 0.58 \wedge T_{remain} \geq 8$):** 8 activations; 6 led to replacement, 2 to continue.
- **Total fleet replacements:** 11 (**Tier 2:** 5, **Tier 3:** 6).

Threshold sensitivity analysis shows that varying each boundary by ±0.03 SoH units changes total fleet replacement count by at most ±2 events and 20-year fleet-average COE by less than 0.003 $/kWh, confirming robustness to small perturbations. When the degradation acceleration factor $\alpha_{deg}$ is varied between 1.5 and 2.0, total replacement count ranges from 13 to 18 events and fleet-average COE from 0.069 to 0.076 $/kWh, demonstrating that qualitative conclusions are robust to plausible uncertainty in SLB degradation rate assumptions.

To test the sensitivity of fleet outcomes to the SoC-window zone boundaries in Equation (12) specifically (as distinct from the penalty-weight sensitivity above and the replacement-trigger sensitivity discussed in Section 2.5.1), the two adjustable boundaries (0.60, 0.54) were each shifted by ±0.03 SoH under an identical random seed and simulation configuration. Across the tested horizon, fleet-average SoH trajectories and cumulative replacement counts differed from the baseline configuration by less than 0.05%, with no observed change in replacement timing. This indicates that fleet-level outcomes are not strongly sensitive to the precise placement of these boundaries within this range, consistent with the SoC/C-rate envelope they define acting as a secondary safety constraint rather than the primary driver of dispatch decisions under the realized load, generation, and price conditions.

The sensitivity of the framework to the penalty weight parameters is examined in Figure 13, which presents heatmaps of Year-1 utilization rate and annual SoH loss across a 5×5 grid of β and γ values. The results confirm that both metrics vary by less than 9 percentage points across the full sweep, demonstrating that the reported performance is robust to ±30% variation in β and γ around their selected values. The replacement trigger activation statistics are visualized in Figure 14, which shows the tier-by-tier breakdown of the 15 trigger activation events (11 of which resulted in actual replacement decisions) and the sensitivity of total replacement count and fleet COE to the degradation acceleration factor $\alpha_{deg}$.

ARTICLE IN PRESS




*Fleet total replacements: 11 (Tier 2: 5 + Tier 3: 6). Threshold sensitivity ±0.03 SoH: ΔLCOE < 0.003 $/kWh, ΔReplacements ≤ 2.*

ARTICLE IN PRESS

**Figure 14.** Replacement trigger statistics. **(a)** Three-tier replacement trigger activation counts and outcomes across all five prosumers over the 20-year simulation (**Tier 1:** 0 activations; **Tier 2:** 7 activations, 5 replacements; **Tier 3:** 8 activations, 6 replacements). **(b)** Sensitivity of total fleet replacements and fleet-average COE to the SLB degradation acceleration factor $\alpha_{deg} \in [1.5 , 2.0]$.

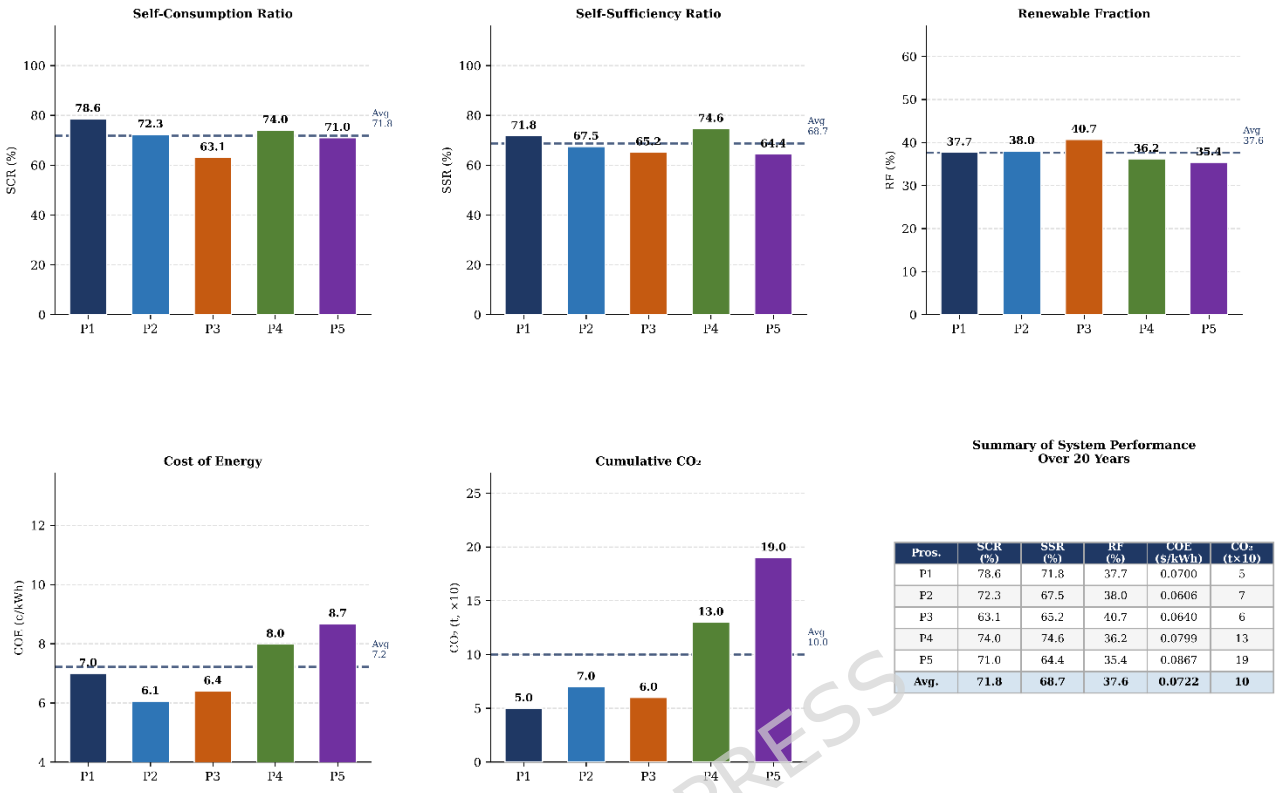
### 3.6. Consolidated System Performance Summary

The multi-metric performance summary presented in Figure 15 consolidates the key performance indicators, SCR, SSR, RF, COE, and cumulative $CO_2$ emissions, for each prosumer across the full 20-year simulation horizon. The summary table embedded in Figure 15 confirms a fleet-average SCR of 71.8% and SSR of 68.7%, with RF values ranging from 35.4% (P5) to 40.7% (P3). Average COE across all prosumers amounts to 0.0722 $/kWh, a figure that lies within the economic viability threshold established in the literature for SLB-based residential storage and is competitive with grid retail prices under the assumed time-of-use tariff structure. Total cumulative $CO_2$ emissions across all prosumers amount to 52 metric tons over 20 years, averaging 10.4 t per prosumer, which translates to a meaningful reduction in carbon footprint relative to a grid-only supply scenario given Turkey's grid carbon intensity of 0.4261 kg/kWh.

Across all five prosumers, the proposed ABM-based EMS framework consistently demonstrates its capacity to navigate the intrinsic trade-off between utilization and longevity that defines second-life battery management. The prosumer-level performance bar charts in Figure 15 reveal that P4 achieves the highest SSR among the five prosumers, consistent with its large ESS allocation and resulting high local supply coverage, while P1 maintains the best balance between SCR and COE efficiency. The differences among prosumers in RF, COE, and emissions outcomes are interpretable through the lens of their respective PSO-assigned system sizes and initial SoH values, reinforcing the conclusion that integrated sizing-and-management co-optimization, rather than sequential or decoupled approaches, is essential for extracting maximum value from heterogeneous SLB fleets. These results collectively establish the technical and economic feasibility of the proposed framework and provide a quantitative foundation for the policy and design guidelines discussed in the following section.

ARTICLE IN PRESS

ARTICLE IN PRESS




**Summary of System Performance Over 20 Years**

| Pros. | SCR (%) | SSR (%) | RF (%) | COE ($/kWh) | $CO_2$ (t×10) |
|---|---|---|---|---|---|
| P1 | 78.6 | 71.8 | 37.7 | 0.0700 | 5 |
| P2 | 72.3 | 67.5 | 38.0 | 0.0606 | 7 |
| P3 | 63.1 | 65.2 | 40.7 | 0.0640 | 6 |
| P4 | 74.0 | 74.6 | 36.2 | 0.0799 | 13 |
| P5 | 71.0 | 64.4 | 35.4 | 0.0867 | 19 |
| **Avg.** | **71.8** | **68.7** | **37.6** | **0.0722** | **10** |

**Figure 15.** Consolidated 20-year system performance summary for all five prosumers: prosumer-level bar charts of SCR, SSR, RF, COE, and cumulative $CO_2$ emissions, with fleet-average summary table.

## 4. DISCUSSION

### 4.1. Interpretation of Key Performance Indicators

The fleet-average COE of 0.0722 $/kWh is competitive with retail grid tariffs under the assumed time-of-use pricing structure and consistent with recent literature reporting COE values of 0.06–0.10 $/kWh for PV-coupled SLB systems [4,17]. The SCR of 71.8% indicates that the majority of PV generation is consumed locally, reducing grid export dependence in a market where the feed-in tariff is substantially below the import price. The SSR of 68.7% confirms that local generation and storage together satisfy approximately two-thirds of prosumer demand, a result consistent with the modeled PV-to-load sizing ratios. The renewable energy penetration factor of 37.6% reflects residual grid imports during low-irradiance periods and trended upward over the 20-year horizon as battery replacement cycles restored effective capacity.

### 4.2. Comparative Evaluation and Mechanism Attribution

The benchmark comparison in Table 2 indicates that, under the simulated 2024 Antalya conditions, full ABM outperforms all three baselines on 20-year COE and fleet SoH while maintaining competitive year-1 SCR. The COE advantage over static-constraint MPC (0.0722 vs. 0.0783 $/kWh) and the lower actual replacement count (11 actual replacements vs. 18

ARTICLE IN PRESS

for static MPC) are attributable to the adaptive constraint mechanism, which moderates degradation in later SoH zones without over-restricting battery access in early years.

The ablation study confirms that neither mechanism, adaptive SoC bounds nor the utilization penalty, achieves the favorable outcome independently. Disabling the utilization penalty causes utilization to fall below 50% for P2 and P3 (underutilization regime risk); disabling adaptive bounds increases annual SoH loss by approximately 1.3 percentage points relative to full ABM. The rule-based EMS achieves comparable year-1 energy routing but incurs 47% more replacement triggers over 20 years, confirming the long-horizon value of degradation-aware scheduling.

The benchmark performance differences across the four configurations are visualized in Figure 16 for direct comparison. The ablation results are presented in Figure 17.

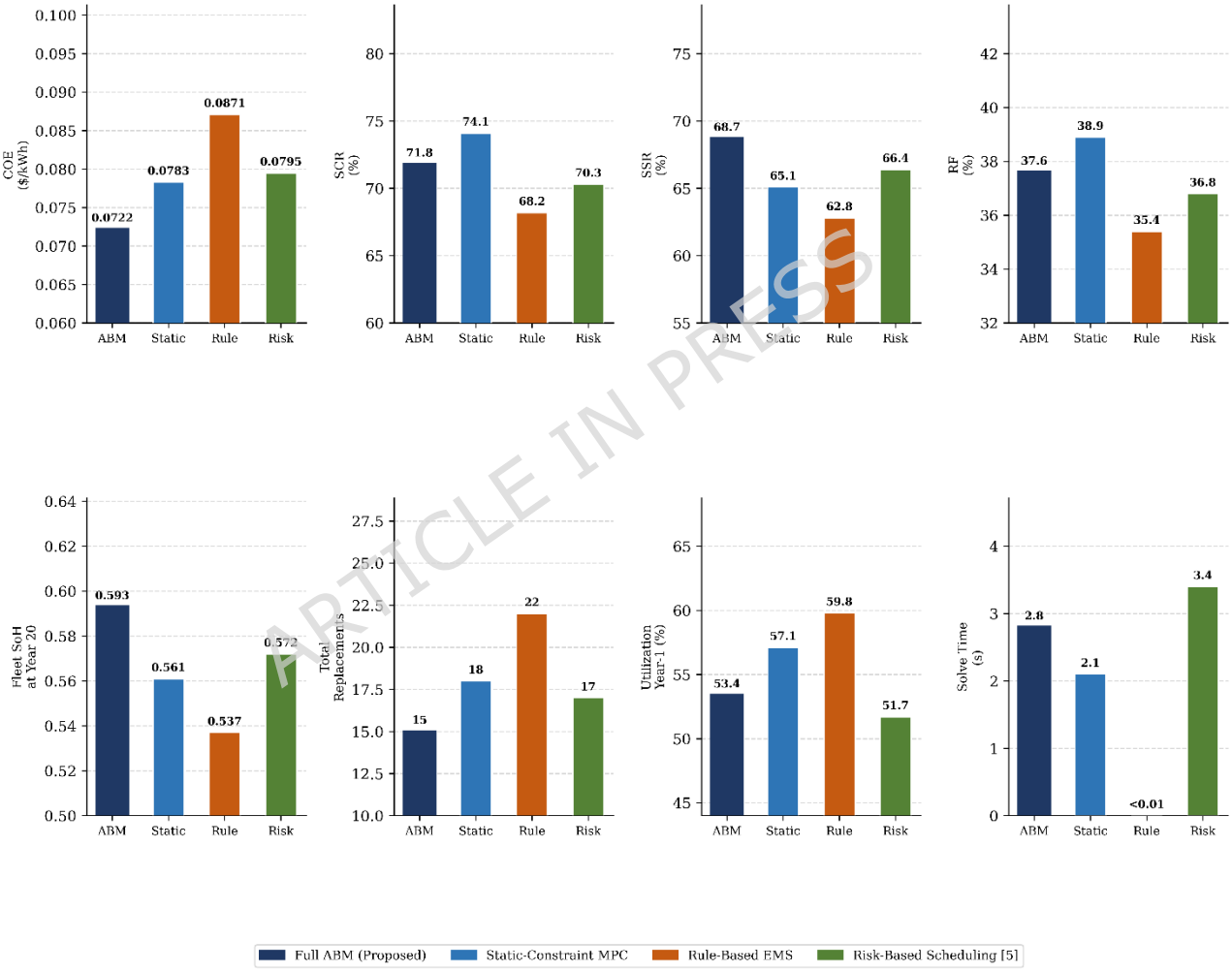



**Figure 16.** Benchmark Comparison. Fleet-average performance metrics of the Full ABM (proposed) framework compared against three baseline configurations (Static-Constraint MPC, Rule-Based EMS, Risk-Based Scheduling [5]) across the 20-year simulation horizon. Metrics: COE, SCR, SSR, RF, fleet SoH at Year 20, replacement triggers, Year-1 utilization, and MPC solve time. Data: 2024 Antalya meteorological and market dataset.

### 4.3. Limitations

ARTICLE IN PRESS

This study has five main limitations. (1) The degradation model (Equations (10)–(11)) does not incorporate temperature-dependent Arrhenius calendar aging kinetics; this simplification is appropriate for Antalya's mild thermal climate (annual mean ~18–20°C) but limits generalizability to thermally variable environments. (2) The residential load profiles are scaled from the Pecan Street (Austin, Texas) dataset to Antalya conditions; for the scaled profiles used in this study, the fleet-average peak-to-average power ratio is 4.34 (range 3.6–5.0) and the load factor is 0.244, with a monthly load-variance coefficient of 9.3% (range 3.6–18.9%) across the five prosumers. A search of the publicly available Turkish residential smart-meter literature did not identify a peer-reviewed source reporting comparable household-level statistics against which these values could be directly benchmarked; this absence is itself noted as an unquantified source of uncertainty, in addition to the qualitative climate and appliance-mix differences between Austin and Antalya. (3) The SoH-zone boundaries used in Equation (12) (0.60, 0.54) were set by engineering judgement rather than fitted to second-life NMC cycling data, although Section 3.5 shows fleet outcomes are not strongly sensitive to ±0.03 perturbations of these values. (4) The forecast-accuracy gap between the proposed AI architectures and a naive persistence baseline is quantified directly (Section 2.3: $R^2$ = 0.726 vs. 0.94 for load, 0.889 vs. 0.987 for PV), but a fully re-optimized persistence-fed ABM configuration analogous to the other Table 3 rows was not completed. (5) The framework is evaluated entirely through computational simulation with no field deployment or hardware-in-the-loop testing; all reported performance figures are simulation-based projections under the stated modeling assumptions and should not be interpreted as empirically confirmed system outcomes.

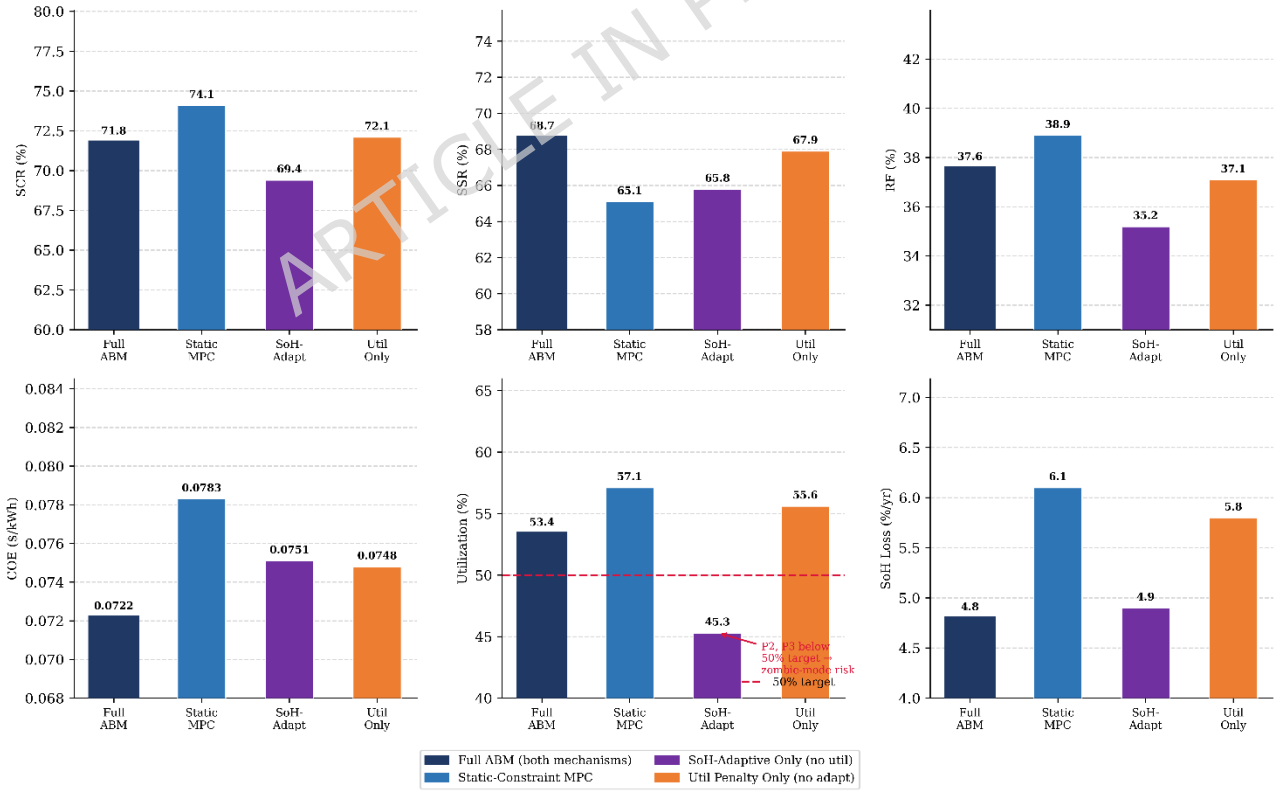



**Figure 17.** Ablation Study.Year-1 fleet-average performance metrics across four ABM mechanism configurations: Full ABM (both mechanisms active), Static-Constraint MPC (no

ARTICLE IN PRESS

adaptive bounds, no utilization penalty), SoH-Adaptive Constraints Only, and Utilization Penalty Only. The red dashed line in the utilization panel marks the 50% minimum throughput target; configurations falling below this threshold are at risk of underutilization.

### 4.4. Directions for Future Work

Several extensions of the present framework would strengthen both its scientific validity and practical deployability. Incorporating Arrhenius-based temperature kinetics into the degradation model (Equations 10–11) would enable application to thermally variable climates and high-C-rate deployment scenarios. Integration of real-time SoH estimation, for example, an extended Kalman filter applied to a first-order equivalent circuit model, would replace the simulation-based degradation tracker and bring the framework closer to hardware deployment. Extension of the NPV-based replacement logic to incorporate stochastic electricity market price scenarios, via robust or chance-constrained optimization, would address the price uncertainty that the current deterministic formulation does not capture. Finally, scaling the framework to multi-community microgrid configurations with shared storage and peer-to-peer energy trading represents a natural progression that could unlock further economic and grid-stability benefits beyond those demonstrated at the prosumer level.

## 5. CONCLUSIONS

This study developed and validated a comprehensive energy management framework for SLB systems integrated with residential photovoltaic installations, addressing a set of interconnected challenges that existing literature has only partially resolved. The starting point of the analysis was the recognition that SLBs cannot be managed as degraded versions of FB; their heterogeneous first-life histories, accelerated aging dynamics, and stochastic remaining useful lives demand a fundamentally different control philosophy, one that treats SoH not as a fixed parameter but as an evolving state that continuously reshapes the operational envelope of the system.

The PSO-based capacity optimization demonstrated that economically optimal ESS sizing for heterogeneous SLB fleets requires direct integration of SoH-dependent cost structures into the objective function. The systematic overprovisioning of nominal capacity relative to FB installations is not a design inefficiency but a rational response to reduced initial usable capacity, and the near-zero correlation between initial SoH and PSO-assigned nominal capacity confirms that the optimizer correctly amortizes degradation risk over the investment horizon rather than treating SoH as a simple capacity multiplier.

The hybrid AI-driven forecasting architecture achieved strong predictive performance across all three target variables, PV generation, electricity price, and load demand, with RMSE and $R^2$ metrics that compare favorably with state-of-the-art benchmarks in each domain. The Monte Carlo dropout-based uncertainty quantification provided well-calibrated 95% prediction intervals, enabling the MPC to incorporate forecast uncertainty into operational decisions without resorting to overly conservative reserve margins that would suppress battery utilization.

The SoH-aware ABM strategy emerged as the central contribution of the framework. By progressively narrowing the SoC operating window and reducing the maximum C-rate as batteries age through defined health zones, the adaptive constraint mechanism significantly moderates the cycle-induced capacity fade that would otherwise condemn SLBs to early

ARTICLE IN PRESS

retirement. Equally important is the utilization penalty mechanism, which prevents the system from entering an underutilization regime, defined as annual throughput below 50% of effective capacity, in which overly conservative degradation protection renders battery participation too infrequent to generate sufficient economic or environmental value. The 20-year simulation results indicate that the fleet's average utilization rate remained at or above the target level for most of the simulated years across the five prosumers, consistent with the intended effect of the penalty formulation.

The NPV-based replacement decision logic contributed to a dimension of economic rationality that is absent from most SLB management frameworks. The three-tier hierarchical structure, encompassing hard EoL enforcement, underutilization prevention, and proactive economic optimization, ensures that replacement decisions reflect the full discounted lifecycle cost of continued operation versus reinvestment, including the degradation-accelerating effects of aging that compound over time. The resulting replacement timelines, averaging three to four events per prosumer over 20 years, are consistent with the expected service life of SLBs under realistic operational stress and confirm that the proposed logic avoids both premature replacement (excessive capital expenditure) and delayed replacement (economic and technical deterioration).

From an environmental perspective, the framework achieved a fleet-wide cumulative $CO_2$ emission total of 52 metric tons over 20 years, equivalent to approximately 0.52 tonnes per prosumer per year, alongside a fleet-average renewable energy penetration factor of 37.6% that trended upward over the operational horizon. These outcomes, derived under 2024 meteorological and market conditions for the five-prosumer Antalya case study, demonstrate measurable $CO_2$ displacement potential relative to a grid-only supply scenario under the Turkish grid emission factor of 0.4261 kg/kWh. This represents a simulation-based lower bound on the environmental benefit of SLB deployment under the modeled conditions, and should be interpreted accordingly rather than as a generalized policy conclusion. On the other hand, the limitations of this study, and the corresponding directions for future work, are summarized in Sections 4.3 and 4.4.

ARTICLE IN PRESS

**Funding**

This study was supported by the Scientific and Technological Research Council of Türkiye (TÜBİTAK) under Grant No. 124E569 within the scope of the 1002-A Short-Term Research Funding Program, as part of the project entitled "Energy Management and Performance Optimization of Second-Life Batteries: Development of Smart Energy Management Systems and Aging Models."

**References**

1. Cheng, M. *et al.* Sustainability evaluation of second-life battery applications in grid-connected PV-battery systems. *J. Power Sources* **550**, 232132 (2022).
2. Kebir, N. *et al.* Second-life battery systems for affordable energy access in Kenyan primary schools. *Sci. Rep.* **13**, 1374 (2023).
3. Salek, F., Resalati, S., Morrey, D., Henshall, P. & Azizi, A. Technical Energy Assessment and Sizing of a Second Life Battery Energy Storage System for a Residential Building Equipped with EV Charging Station. *Appl. Sci.* **12**, 11103 (2022).
4. Li, R., Hassan, A., Gupte, N., Su, W. & Zhou, X. Degradation Prediction and Cost Optimization of Second-Life Battery Used for Energy Arbitrage and Peak-Shaving in an Electric Grid. *Energies* **16**, (2023).
5. Zhang, Y., Zhu, J., Xu, Y., Zhou, R. & Dong, Z. Y. Risk-based Two-stage Optimal Scheduling of Energy Storage System with Second-life Battery Units. *CSEE J. Power Energy Syst.* **9**, 529–538 (2023).

ARTICLE IN PRESS

6. Spindlegger, A. *et al.* Environmental performance of second-life lithium-ion batteries repurposed from electric vehicles for household storage systems. *Sustain. Prod. Consum.* **54**, 227–240 (2025).
7. Kebede, A. A. *et al.* Optimal sizing and lifetime investigation of second life lithium-ion battery for grid-scale stationary application. *J. Energy Storage* **72**, 108541 (2023).
8. Tanjil Sarker, M., Al Qwaid, M., Ramasamy, G. & Hussein Saleh Mohammed Haram, M. Performance Evaluation of Second-Life EV Batteries for Off-Grid Solar Energy Storage System. *IEEE Access* **13**, 148365–148373 (2025).
9. Bhatt, A., Ongsakul, W. & Madhu M., N. Optimal techno-economic feasibility study of net-zero carbon emission microgrid integrating second-life battery energy storage system. *Energy Convers. Manag.* **266**, 115825 (2022).
10. Deng, Y., Zhang, Y., Luo, F. & Mu, Y. Hierarchical energy management for community microgrids with integration of second-life battery energy storage systems and photovoltaic solar energy. *IET Energy Syst. Integr.* **4**, 206–219 (2022).
11. Steckel, T., Kendall, A. & Ambrose, H. Applying levelized cost of storage methodology to utility-scale second-life lithium-ion battery energy storage systems. *Appl. Energy* **300**, 117309 (2021).
12. Di Rienzo, R. *et al.* A novel methodology to study and compare active energy-balance architectures with dynamic equalization for second-life battery applications. *J. Energy Storage* **73**, 108772 (2023).
13. Azaroual, M., Ouassaid, M. & Maaroufi, M. Chapter 5 - Model predictive control-based energy management strategy for grid-connected residential photovoltaic–wind–battery system. in *Renewable Energy Systems* (eds. Azar, A. T. & Kamal, N. A.) 89–109 (Academic Press, 2021). doi:https://doi.org/10.1016/B978-0-12-820004-9.00014-0.
14. Hu, Y., Li, Z. & Cui, J. An economic model predictive control strategy for EV-integrated microgrids considering battery degradation. *Energy* **335**, 138205 (2025).
15. Li, Y., Vilathgamuwa, D. M., Quevedo, D. E., Lee, C. F. & Zou, C. Ensemble Nonlinear Model Predictive Control for Residential Solar Battery Energy Management. *IEEE Trans. Control Syst. Technol.* **31**, 2188–2200 (2023).
16. Arcos–Aviles, D., Salazar, A., Rodriguez, M., Martinez, W. & Guinjoan, F. Model predictive control-based energy management system for an isolated electro-thermal microgrid in the Amazon region of Ecuador. *Energy Convers. Manag.* **310**, 118479 (2024).
17. Cao, Z., Kurdkandi, N. V., Jia, S. & Mi, C. Multi-timescale electricity cost optimization for commercial buildings using EV second-life battery as energy storage systems. *eTransportation* **27**, 100515 (2026).
18. Haram, M. H. S. M., Sarker, M. T., Ramasamy, G. & Ngu, E. E. Second Life EV Batteries: Technical Evaluation, Design Framework, and Case Analysis. *IEEE Access* **11**, 138799–138812 (2023).
19. Cheng, M., Zhang, X., Ran, A., Wei, G. & Sun, H. Optimal dispatch approach for second-life batteries considering degradation with online SoH estimation. *Renew. Sustain. Energy Rev.* **173**, 113053 (2023).
20. Lacap, J., Park, J. W. & Beslow, L. Development and Demonstration of Microgrid System Utilizing Second-Life Electric Vehicle Batteries. *J. Energy Storage* **41**, 102837 (2021).
21. Gao, W., Cao, Z., Kurdkandi, N. V., Fu, Y. & Mi, C. Evaluation of the second-life potential of the first-generation Nissan Leaf battery packs in energy storage systems. *eTransportation* **20**, 100313 (2024).
22. Meng, Q., He, Y., Hussain, S., Lu, J. & Guerrero, J. M. Design and optimization of solar photovoltaic microgrids with adaptive storage control for residential standalone systems. *Energy Reports* **14**, 989–997 (2025).
23. Song, Z., Nazir, M. S., Cui, X., Hiskens, I. A. & Hofmann, H. Benefit assessment of second-life electric vehicle lithium-ion batteries in distributed power grid applications. *J. Energy Storage* **56**, 105939 (2022).
24. Rehman, J. A., Lin, Z. & Fleming, J. Model Predictive Control for Energy Management of Microgrids Considering Battery Degradation. in *2024 UKACC 14th International*

ARTICLE IN PRESS

ARTICLE IN PRESS

*Conference on Control (CONTROL)* 205–206 (2024). doi:10.1109/CONTROL60310.2024.10531978.
25. Shehzad, M. & Gueniat, F. Modeling and Optimal Control of Energy Storage Strategy For Battery Life Extension Via Model Predictive Control. in *2021 European Control Conference (ECC)* 1981–1986 (2021). doi:10.23919/ECC54610.2021.9654971.
26. Martinez-Laserna, E. *et al.* Battery second life: Hype, hope or reality? A critical review of the state of the art. *Renew. Sustain. Energy Rev.* **93**, 701–718 (2018).
27. Vykhodtsev, A. V, Jang, D., Wang, Q., Rosehart, W. & Zareipour, H. Physics-Aware Degradation Model of Lithium-ion Battery Energy Storage for Techno-Economic Studies in Power Systems. *IEEE Trans. Sustain. Energy* **15**, 316–327 (2024).
28. Yang, J., Beatty, M., Strickland, D., Abedi-Varnosfaderani, M. & Warren, J. Second-Life Battery Capacity Estimation and Method Comparison. *Energies* **16**, 3244 (2023).
29. La Tona, G., Luna, M. & Di Piazza, M. C. A Multi-Objective Optimization-based EMS for Residential Microgrids Considering Battery SoH. in *IECON 2022 – 48th Annual Conference of the IEEE Industrial Electronics Society* 1–6 (2022). doi:10.1109/IECON49645.2022.9968553.
30. Shabani, M. & Yan, J. Optimization and evaluation of operational and economic performance of grid-connected battery storage at different stages of battery health. *Energy Convers. Manag. X* **27**, 101113 (2025).
31. Poblete, P. *et al.* Dual-Stage MPC for SoC Balancing in Second-Life Battery Energy Storage Systems Based on Delta-Connected Cascaded H-Bridge Converters. *IEEE Trans. Power Electron.* **40**, 500–515 (2025).
32. Zhou, K., Fei, Z. & Hu, R. Hybrid robust decentralized optimization of emission-aware multi-energy microgrids considering multiple uncertainties. *Energy* **265**, 126405 (2023).
33. Schmitt, T., Engel, J. & Rodemann, T. Regression-Based Model Error Compensation for a Hierarchical MPC Building Energy Management System. in *2023 IEEE Conference on Control Technology and Applications (CCTA)* 1–8 (2023). doi:10.1109/CCTA54093.2023.10252861.
34. Vašak, M. *et al.* Modular Hierarchical Model Predictive Control for Coordinated and Holistic Energy Management of Buildings. *IEEE Trans. Energy Convers.* **36**, 2670–2682 (2021).
35. Iqbal, H., Sarwar, S., Kirli, D., Shek, J. K. H. & Kiprakis, A. E. A survey of second-life batteries based on techno-economic perspective and applications-based analysis. *Carbon Neutrality* **2**, 8 (2023).
36. Biskupski, J. A. Techno-Economics of Using Second Life BEV Traction Batteries as BESS in Domestic RES Installations. *Energy Storage Appl.* **2**, (2025).
37. Akram, M. N. & Abdul-Kader, W. Supporting Sustainable Development Goals with Second-Life Electric Vehicle Battery: A Case Study. *Sustainability* **17**, 6307 (2025).
38. Meng, X. *et al.* Dissipativity-Based Multiport Stability Root-Cause Identification and Mitigation for Solid-State Transformers. *IEEE Trans. Ind. Electron.* **73**, 9850–9862 (2026).
39. Neubauer, J. & Pesaran, A. The ability of battery second use strategies to impact plug-in electric vehicle prices and serve utility energy storage applications. *J. Power Sources* **196**, 10351–10358 (2011).
40. Wang, H., Ngaopitakkul, A. & Yoomak, S. SOH- and Temperature-Aware Adaptive SOC Boundaries for Second-Life Li-Ion Batteries in Off-Grid PV–BESSs. *Computation* **14**, (2026).
41. Farakhor, A. *et al.* Economic optimal power management of second-life battery energy storage systems. *J. Energy Storage* **133**, 117680 (2025).